UNIVERSITY OF COPENHAGEN
FACULTY OF SCIENCE

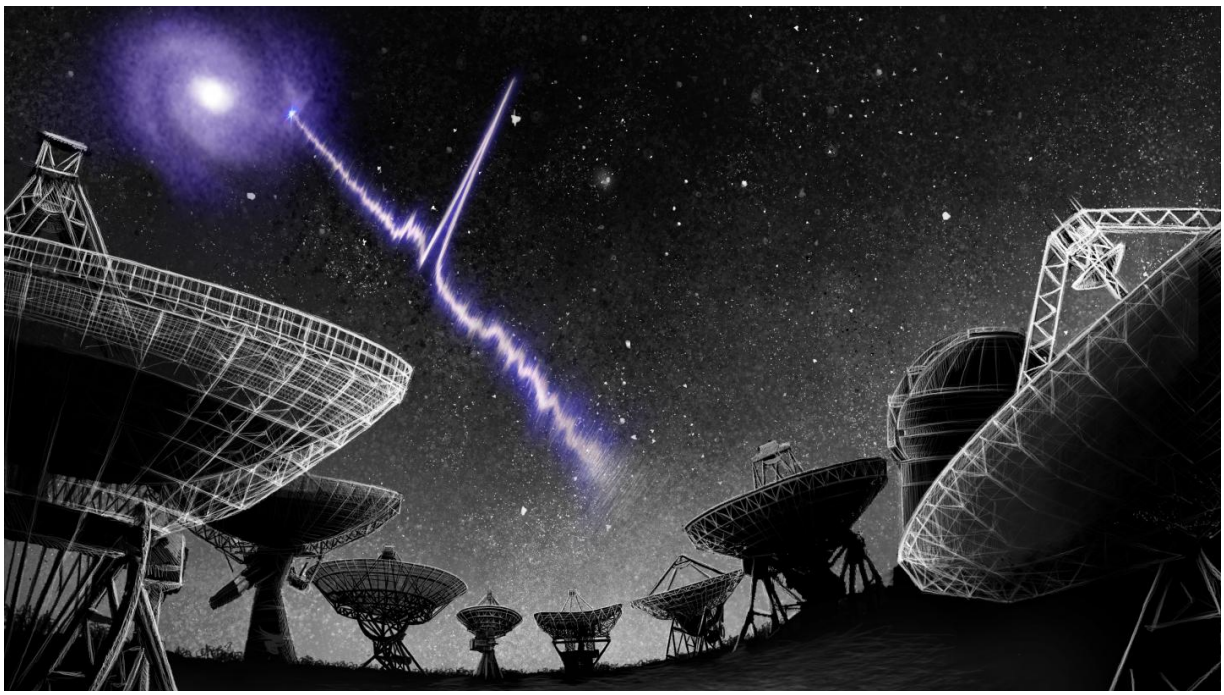

Master Thesis

Jo Verwohlt Damm

Future Cosmological Constraints on Dark Matter

Gravitational Lensing of Fast Radio Bursts

Supervised by Radosław Wojtak & Steen H. Hansen

Handed in: 14th of October 2021

Abstract

The physical nature of dark matter is largely unknown. In the standard cosmological model, a scenario where all dark matter is in the form of cold dark matter (CDM) is generally preferred, however there remains an open window that allows for dark matter in the form of primordial black holes (PBHs) with masses of 20-100 $M_\odot$ as well as warm dark matter (WDM). Extragalactic transients on millisecond scale - such as Fast Radio Bursts (FRBs), propose the opportunity to study the nature of dark matter when they are gravitationally lensed by PBHs and dark matter halos. In this thesis, we investigate how gravitationally lensed FRBs can be used to constrain dark matter. We find that for an FRB distribution similar to the recently published CHIME/FRB catalogue and for a realistic detection rate of 10^4 FRBs per year, we can constrain the fraction of dark matter in the form of PBHs to 0.08 $\%$ for $M_L > 20$ $M_\odot$ if less than one out of 10^4 FRBs are lensed. We find that the constraints on dark matter particle mass, as probed by the halo mass function, are much weaker and that it is essentially impractical to distinguish between a CDM and WDM scenario. 10^4 FRB detections are not sufficient in constraining dark matter particle mass.

Contents

1 Introduction

13.7 billion years ago, the Universe was created in the Big Bang. Energy and matter were streaming around the Universe, and the Universe expanded very rapidly.

The very early Universe was radiation-dominated and the existence of matter created a hot and dense environment called the primordial plasma. Atoms existed in the form of plasma, electrons were decoupled from the atomic nuclei, and as photons would scatter off the free electrons, light could not travel very far.

As the Universe expanded, matter cooled down, with electrons and nuclei eventually recombining to form neutral atoms. As a result of recombination, photons were no longer scattered by free electrons, and the Universe became transparent. At this particular time, the Universe enters the matter-dominated epoch. Matter and its gravitational interactions would dominate how the Universe would start to clump together, and gas collapsed to form galaxies and stars.

We normally consider matter to be anything that constitutes an atom. The electrons in the shells, the protons and neutrons in the nuclei and the even smaller quarks that make up the protons and neutrons. Matter is what comprises the smallest dust grains, the massive galaxies and the brightest stars. However, matter is not only the massive objects that we can see. In the last century, it's become evident that there's seemingly more mass in the universe than what we are able to see - and it appears to make up about 85% of mass in the Universe. This invisible mass is known as dark matter. Throughout the history of astronomy, the primary source of information about the Universe has been light. This renders the process of observing and characterising dark matter a particularly tricky endeavour. As the primary attribute of dark matter is its mass, we can observe it indirectly via its gravitational effects.

In recent years, gravitational lensing has emerged as a particularly useful tool for astrophysicists. Gravitational lensing occurs when a massive object bends space-time and light behind the lensing object is forced to travel on a curved path. Sometimes there will be multiple paths that the light can travel, and if the paths have different lengths, the light will arrive at the observe with a time delay between the different images - they arrive separated by a gravitational time delay. Gravitational lensing does not discriminate between types of matter, and gravitational time delay can be used to determine the mass of the lensing objects. For instance, it can be employed to determine the full mass of a galaxy cluster, including the dark matter within.

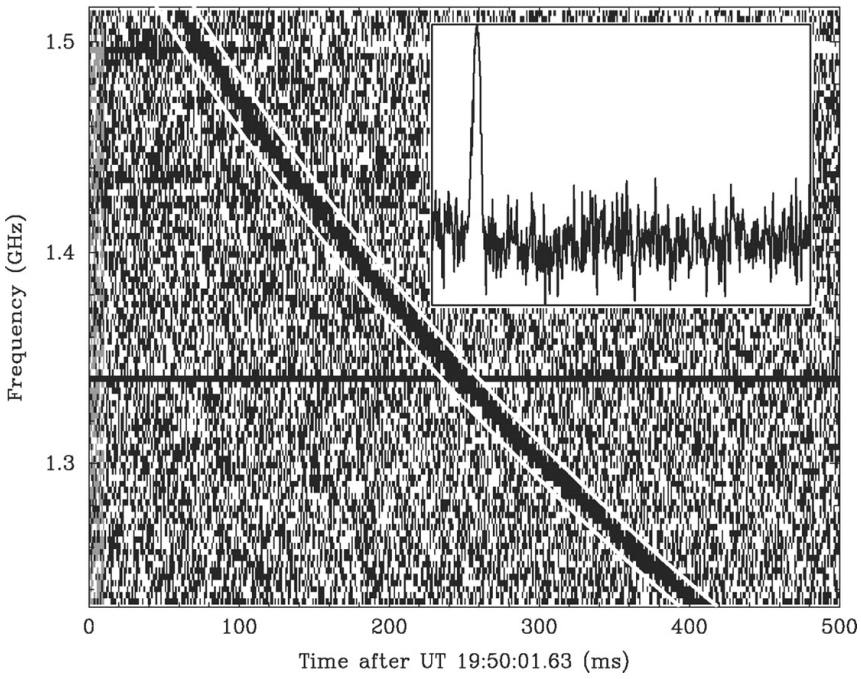

Figure 1: The first detection of a Fast Radio Burst by Lorimer et al. (2007) The sharp peak is associated with the presence of an FRB.

The fairly new discovery of Fast Radio Bursts - bright radio pulses on millisecond scale - might shed some light on the nature of dark matter. These pulses originate from far across the Universe and have a high probability of being lensed by dark matter on their way to Earth. Their short time duration make them a specially interesting tool for dark matter characterisation as it makes it possible to investigate objects on smaller mass scales. This will allow us to investigate dark matter in the form of primordial black holes and possibly between dark matter particles of different masses.

2 Background

2.1 Dark Matter

The current paradigm in astrophysics and cosmology favours a scenario with the existence of dark matter. In 1933, Zwicky identified how galaxies in the Coma cluster moved much faster than expected if their mass was related to velocities via the virial theorem (Zwicky, 1933). It seemed like the cluster was missing some mass, that could not be seen through electromagnetic observations. The cluster could not just be made up of galaxies and gas. In 1970, similar effects were observed on galactic scales by Rubin and Ford (Rubin & Ford, 1970). Stars and gas could not be the only things that constitute a galaxy - there must be some missing mass in galaxies as well. This observation contributed in substantiating the theory of dark matter.

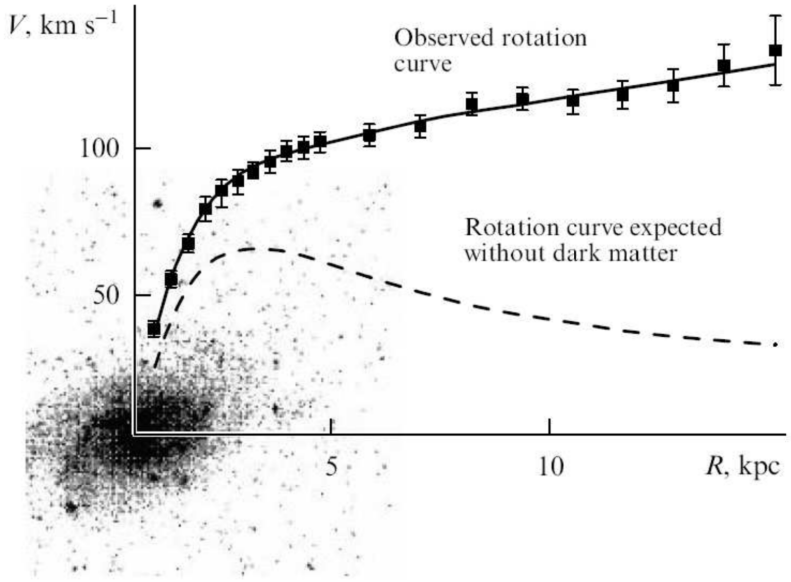

Figure 2: The rotation curve of the M 33 galaxy. Figure adapted from Zasov et al. (2017).

The existence of dark matter becomes particularly necessary when we consider the rotation curve of spiral galaxies. From the dynamics of circular motion around mass centre, we expect that the rotational velocity corresponds to the mass within the given radius. As we go further away from the centre of the galaxy, the density of stars and gas decreases, and one would expect the rotational velocity to decrease as well - but instead we see that the rotational velocity on average flattens out, as depicted in Figure 2). From the rotation curve, it can be deduced that the missing matter is in a dark halo around the galaxy (Longair, 2007).

We describe the Universe through the cosmological principle, which states that the Universe is homogeneous and isotropic on sufficiently large scales. In general, a large region of the Universe seems to have a smooth distribution of luminous matter, but on smaller scales, the Universe appears lumpy, as galaxies clump together, forming groups of galaxies and clusters. These structures, as well as super clusters, filaments and voids, are sometimes referred to as the cosmic web. Cosmological simulations have shown that the morphology of the cosmic web is dictated by the presence of a considerable amount of dark matter in the Universe (Bond et al., 1996).

Since most properties of dark matter are unknown, the nature of dark matter is up for debate and as yet unresolved. Dark matter candidates have been proposed from the smallest types of particles known as axions with a rest mass of 10^{-5} eV to the largest candidates being primordial black holes with masses up to 10^{5} $M_{\odot}$.

2.1.1 Dark Matter Models

We distinguish between models of baryonic and non-baryonic dark matter. Baryonic matter refers to the ordinary matter constituted by neutrons, protons, electrons and black holes. In contrast, non-baryonic refers to everything else. At this moment, all dark matter models are based on non-baryonic dark matter.

Another distinction in dark matter models is whether the dark matter is hot or cold. This characteristic depends on how fast the particles were moving when they decoupled, and affects cosmic structure formation. In cosmology, we generally assume the so-called ΛCDM model that describes a Universe dominated by dark energy and cold dark matter (CDM) (Ryden, 2003).

Cold Dark Matter

Cold dark matter particles are created in the very early Universe. They decoupled early in the Universe after becoming non-relativistic. This is the principal quality of CDM. That CDM particles are cold - that they were non-relativistic at decoupling - means that small-scale structure will not be suppressed by free streaming, since density fluctuations can exist on all scales in the early Universe. These density fluctuations will eventually collapse under the action of gravity to form structures. We will revisit this process in a future section when discussing cosmic structure formation and the halo mass function.

One of the popular candidates to constitute CDM is weakly interacting massive particles (WIMPs) with a mass round 10 GeV to 1 TeV. Such a particle could be the supersymmetric partner of the graviton, known as the gravitino, or the supersymmetric partner of the photon - the photino.

Another CDM candidate comprises axions, which are hypothetical bosons. Axions are proposed to be small particles with a rest mass at 10^{-2} to 10^{-5} eV, such that an axion is currently the candidate with the smallest mass. These small masses imply that they must have originated when the Universe had a temperature around 10^{12} K. Their origin from when the Universe had a temperature around 10^{12} K. Massive astrophysical halo objects (MACHOs), such as primordial black holes (PBHs), are also considered a CDM candidate. .

Primordial Black Holes

Massive astrophysical halo objects (MACHOs) is another type of object that emits very little to no radiation and could constitute dark matter. In principle it could be any class of darker object such as neutron stars and brown dwarfs, as well as black holes. An exciting candidate for dark matter in the form of MACHOs is primordial black holes (PBHs).

PBHs are formed in the radiation-dominated epoch and is consequently classified as non-baryonic dark matter and a possible candidate for CDM (Carr et al., 2020). PBHs could have formed in the early Universe if certain regions were overdense or if expansion rate was lower, and the regions would re-collapse gravitationally (Carr & Hawking, 1974).

In principle, PBHs could be formed on a large mass scales ranging from 10^{-7} to 10^{5} $M_{\odot}$, but different physical and observational arguments have constrained the mass of PBHs. There is a small open window between 20 to 100 $M_{\odot}$ for at least a significant fraction of dark matter to be in the form of PBHs. This is shown in Figure 3 as area C. PBHs with mass below 20 $M_{\odot}$ are excluded by microlensing effects on stars. If dark matter exists as PBHs in the galactic halo in galaxies, we should be able to observe its presence, but there is a lack of observations of such microlensing effects on stars. On larger mass scales, dynamical effects can be used to constrain the possible mass scale of PBHs. This is a particularly strong argument when we consider wider binaries in galaxies. If dark matter is in the form PBHs with a mass above 100 $M_{\odot}$, wide binaries would be perturbed (Carr & Kühnel, 2020). In the 20 to 100 $M_{\odot}$ window, it has been argued that the formation of PBHs will distort the CMB spectrum (see PA region in

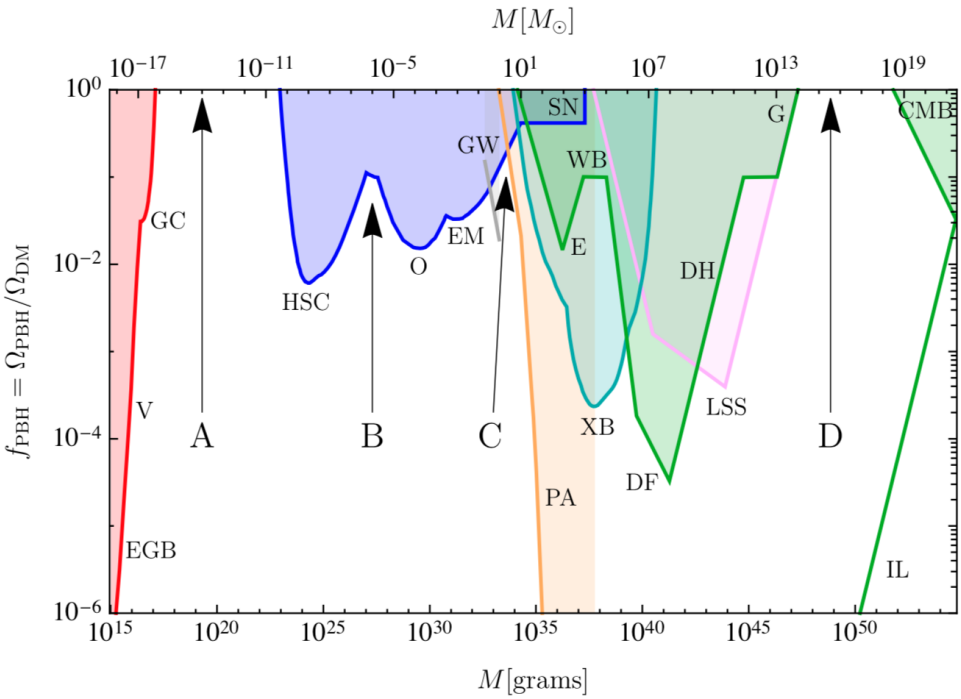

Figure 3: Constraints on the fraction of dark matter in the form of PBHs. Figure adapted from Carr & Kühnel (2020). Multiple mass scales are ruled out by: evaporation (red), lensing (blue), gravitational waves (GW, grey), dynamical effects (green), accretion (light blue), CMB distortions (PA, yellow), and large scale structures (pink). There is open mass windows in area A, B, C, and D.

Figure 3). However, this argument is influenced by different assumptions and is not as strong as the previously mentioned constraints.

In 2016, the Laser Interferometer Gravitational-Wave Observatory (LIGO) detected gravitational waves from a merging event of two black holes (Abbott et al., 2016). The masses of these two black holes were measured to both be around $\sim 30\ M_\odot$. So were they in fact PBHs? Could this be the first direct detection of dark matter? Multiple research articles have since proposed the possiblity that LIGO might have actually detected dark matter in the form of PBHs (Bird et al., 2016).

Warm Dark Matter

Let us first consider the hot dark matter (HDM) scenario. HDM particles are in the form of standard neutrinos with a mass at 10 eV. They become non-relativistic at redshift z = 2×10^4, so

they were highly relativistic when they decoupled (Longair, 2007). Observations of large-scale structures in the local Universe do not agree with the existence of HDM, since we do observe structures on scales that would have been erased by free streaming of HDM particles. However, a less extreme scenario, the so-called Warm Dark Matter (WDM), could still be a possibility. In the WDM scenario, the dark matter particles still have higher velocities when they decouple but they only escape density fluctuations on smaller scales. On larger scales, they will share the same properties as CDM. The particle mass of WDM corresponds to the particle's velocity and temperature and consequently the scale of dark matter halos.

Lyman-α forest data have constrained WDM particle masses to be larger than 3.5 keV (Viel et al., 2005). In this thesis, we will examine WDM particles on a similar mass scale and predict how FRBs lensed by dark matter halos potentially make an analogous constraint.

2.2 Structure Formation

Structure formation refers to how galaxies, galaxy clusters, and large-scale structures are formed from small density fluctuations in the early Universe.

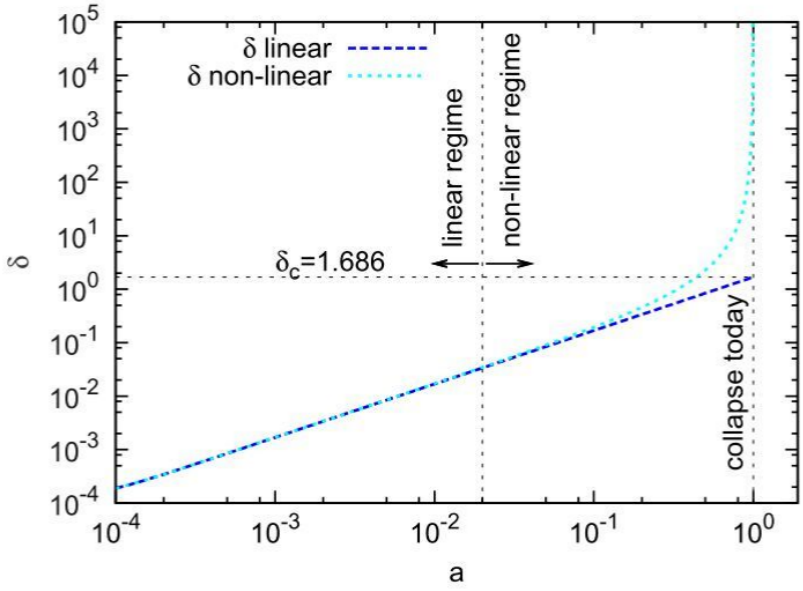

Figure 4: Perturbations described by on-linear growth collapse when linear theory exceeds the critical density $\delta_c = 1.686$. Figure adapted from Pace et al. (2010).

The fluctuations can be described as perturbations in an homogeneous fluid:

$$\delta(\mathbf{x}) = \frac{\rho(\mathbf{x}) - \rho_0}{\rho_0} \tag{1}$$

where $\rho(\mathbf{x})$ is the energy density in an area in the universe and ρ_0 is the average energy density (Longair, 2007). This means that δ is negative for an underdense region and posivtive for an overdense region. When the perturbations are still small, i.e. $\delta \ll 1$, the growth can be described using linear perturbation theory. As the perturbations grow larger, they can no longer be described linearly. Fully non-linear description of the structure formation predicts that a spherical overdense region collapses and forms as halo when linear theory exceeds a critical density of $\delta_c = 1.686$ will collapse (Pace et al., 2010).

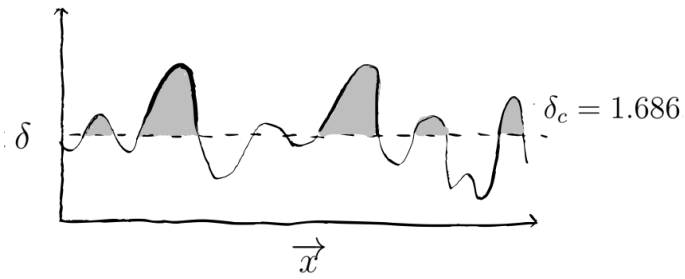

Figure 5: Drawn illustration of how the density perturbations greater than the critical density $\delta = 1.686$ will collapse and form halos.

The two-point correlation function describes the probability of finding two random galaxies within a given distance. It describes how matter is distributed in the Universe, i.e. how lumpy the Universe is. The two-point correlation function is connected to the density contrast $\delta(x)$:

$$\xi(r) = \langle \delta(\mathbf{x}) \delta(\mathbf{x} + \mathbf{r}) \rangle. \tag{2}$$

If we assume that dark matter halos are contained within galaxies, the latter will be tracers for dark matter halos.

We can define the Fourier transformation for $\delta(r)$:

$$\delta(r) = \frac{V}{(2\pi)^3} \int \delta_k e^{-ik \cdot r} \mathrm{d}^3 k \tag{3}$$

$$\delta_k = \frac{1}{V} \int \delta(r) e^{-ik \cdot r} \mathrm{d}^3 x. \tag{4}$$

Between Fourier transform pairs, it follows that:

$$\frac{1}{V}\int \delta^2(r)d^3x = \frac{V}{(2\pi)^3}\int |\delta_k|^2 \mathrm{d}^3k, \tag{5}$$

where $|\delta_k^2|$ is known as the **power spectrum**:

$$P(k) = |\delta_k|^2. \tag{6}$$

The two-point correlation function can be expressed in terms of δ_k, and therefore, the power spectrum:

$$\xi(r) = \frac{V}{(2\pi)^3}\int |\delta_k|^2 e^{ik\cdot r}\mathrm{d}^3k = \frac{V}{(2\pi)^3}\int P(k)e^{ik\cdot r}\mathrm{d}^3k. \tag{7}$$

The power spectrum relates δ, the difference between the local density and the average density in the Universe, to cosmological scales.

Since the power spectrum describe density fluctuations on different scales and these fluctuations give rise to halos via gravitational collapse, the power spectrum can be related to the number of halos at different mass scales.

2.3 Halo Mass Function

In the CDM model, structures form through hierarchical clustering, where smaller scale objects are formed first, followed by the subsequent formation of larger structures.

The number of halos in a comoving volume can be related to their mass via the halo mass function (HMF). The CDM model predicts that the number of halos decreases with mass approximately as a power law: $\frac{\mathrm{d}n}{\mathrm{d}m} \propto M^{-1.8}$.

The HMF is defined by a fitting function $f(\sigma)$:

$$\frac{\mathrm{d}n}{\mathrm{d}\ln M} = M \times \frac{\rho_0}{M^2} f(\sigma)\left|\frac{\mathrm{d}\ln\sigma}{\mathrm{d}\ln M}\right|, \tag{8}$$

where ρ_0 is the mean density of the Universe and σ is the root mean square within a sphere of a given radius R (Murray et al., 2013a). We adopt the conventional value of $R = 8h^-$ Mpc, in accordance with the cosmological σ_8.

2.3.1 Press-Schechter Formalism

We can simplify the formation of halos by assuming that they collapse spherically and that the perturbations follow a Gaussian distribution with mean equal to zero and variance σ^2:

$$\rho(\delta) = \frac{1}{\sqrt{2\pi}\sigma(M)} \exp\left[-\frac{\delta^2}{2\sigma^2(M)}\right], \tag{9}$$

and that $M \propto \rho_0 R^3$ (Longair, 2007).

Analytical work by Press & Schechter (1974) resulted in the following fitting function:

$$f(\sigma) = \sqrt{\frac{2}{\pi}}\frac{\delta_c}{\sigma} \exp\left(-\frac{\delta_c^2}{2\sigma^2}\right), \tag{10}$$

where δ_c is the critical linearly evolved overdensity that will cause a spherical collapse.

N-body simulations that allow for ellipsoidal collapse find that the Press-Schechter fitting function overestimates the abundance of lower mass halos, while underestimating the abundance of higher mass halos (Murray et al., 2013a).

For a CDM scenario, the fitting function is adapted from simulations by Tinker et al. (2008):

$$f_T(\sigma, z) = A\left[\left(\frac{b}{\sigma}\right)^a + 1\right] \exp\left(-\frac{c}{\sigma^2}\right), \tag{11}$$

with the following parameters given by:

$$A = 0.186(1+z)^{-0.14}$$
$$a = 1.47(1+z)^{-0.15}$$
$$b = 0.3(1+z)^{-0.084}$$
$$c = 1.036(1+z)^{-0.024}.$$

2.3.2 Warm Dark Matter

For WDM, we expected that free streaming will suppress halos at lower masses. Free streaming of WDM particles in the early Universe would disperse the density perturbations on smaller scales so that they do not collapse into what would have been low mass halos.

The WDM effects result in an additional transfer function in the power spectrum:

$$P(k) = P_{\mathrm{CDM}} T_K^{X^2}. \tag{12}$$

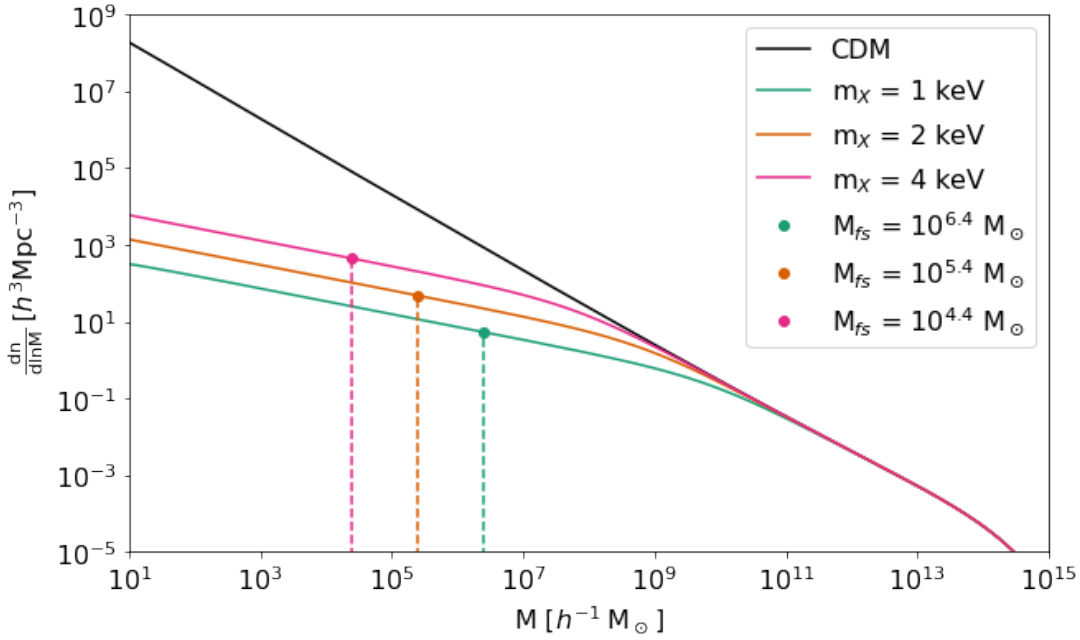

Figure 6: Halo mass function for CDM and WDM of different particle mass m_X. Calculated using `hmfcalc`. The dots show the free streaming mass for each particle type of WDM. For masses below the free streaming mass $M_{\rm fs}$, no halos are formed.

A widely adopted transfer function is provided by Murray et al. (2013b):

$$T_k^X = \left[1 + (\alpha k)^{2\nu}\right]^{-\frac{5}{\nu}}, \tag{13}$$

where $\nu = 1.2$ and α is given by:

$$\alpha = 0.048 \left(\frac{\Omega_X}{0.4}\right)^{0.15} \left(\frac{h}{0.65}\right)^{\frac{1}{3}} \left(\frac{1}{m_X}\right)^{1.15} \left(\frac{1.5}{g_X}\right)^{0.29}, \tag{14}$$

where m_X is the particle mass in keV, Ω_X is the current fractional density of the WDM particle, and g_X is the abundance of species relative to photons.

The computational package `hmfcalc` describes how the HMF changes with WDM particle mass, but does not account for structures that are confined by the lighter WDM particles. Particles with smaller mass will have a higher velocity when they decouple. this results in a larger effective free streaming scale:

$$\lambda_{\rm fs}^{\rm eff} = 0.049 \times \left[\frac{m_{\rm X}}{\rm keV}\right]^{-1.11} \left[\frac{\Omega_{\rm X}}{0.25}\right]^{0.11} \left[\frac{h}{0.7}\right]^{1.22} {\rm Mpc}\, h^{-1} \tag{15}$$

The free streaming mass scale is the minimum mass scale for halo formation for a given WDM particle mass, i.e. $\rm M < M_{fs}$ (Schneider et al., 2012).

$$M_{\rm fs} = \frac{4\pi}{3}\bar{\rho}\left(\frac{\lambda_{\rm fs}^{\rm eff}}{2}\right)^3 \tag{16}$$

In Figure 6, we show the halo mass function for CDM and different types of WDM. The dots mark the free streaming mass $M_{\rm fs}$ for each WDM particle of 1 keV, 2 keV, and 4 keV, respectively. To the left of these points, halos are not formed. Simulations show that this is more of a smooth transition, but in this thesis we will treat it as a strict cut off such that $\frac{dn}{d\ln M}\,(M < M_{\rm fs}) = 0$.

2.3.3 Sub-halos

Cosmological simulations of structure formation within a ΛCDM Universe propose that CDM halos do not exhibit a simple and smooth structure, but that multiple sub-halos on all mass scales reside within dark matter halos. Smaller dark matter structures collapse at high redshift and accrete to form large dark matter halos (Madau et al., 2008). The sub-halos have a sufficiently large density to maintain their gravitationally bound structure as they merge with larger halos.

The number of sub-halos within a host halo is given by the unevolved sub-halo mass function (USMF):

$$F\left(\frac{M_{\rm acc}}{M_{\rm host}}\right) = \frac{dN_{\rm sub}}{d\ln(M_{\rm acc}/M_{\rm host})} = a\left(\frac{M_{\rm acc}}{M_{\rm host}}\right)^b \exp\left[-c\left(\frac{M_{\rm acc}}{M_{\rm host}}\right)^d\right], \tag{17}$$

where $M_{\rm acc}$ is the sub-halo mass at accretion, $M_{\rm host}$ is the host halo mass, $N_{\rm sub}$ is the number of sub-halos, while a,b,c, and d are the fitting parameters optimised via simulations to have the following best-fit values Li & Mo (2009): $a = 0.20$, $b = -0.76$, $c = 6.00$, $d = 3.20$. This function gives the upper limit on the number of sub-halos, if all accreted mass results in sub-halos. In reality, it is very likely that not all sub-halos can withstand the tidal forces of a merger.

2.4 Cosmology and Distance Measures

This section is based on equations in Hogg (1999). When we talk about distance in cosmology, it does not refer to one specific kind. As the Universe is expanding, the distance between objects will change. It takes time for light that is emitted by an object to reach an observer on Earth. As astronomers, we are always looking back in time.

To describe how fast space is expanding, we use the Hubble parameter $H(t)$ as the proportionality constant between the distance and the recession speed. The Hubble parameter $H(t)$ changes with time. The Hubble constant H_0 corresponds to the present-day value of the Hubble parameter. In this thesis, we adopt the WMAP9 cosmology (Hinshaw et al., 2013), with $H_0 = 69.32$ km s^{-1} Mpc^{-1}. The Hubble constant can be expressed as:

$$H_0 = \frac{v}{d}, \tag{18}$$

where v is the recession velocity and d is the distance.

As photons propagate through space, the wavelengths are stretched out by the expanding space and the light is redshifted by z:

$$z = \frac{\nu_{\text{emitted}}}{\nu_{\text{observed}}} - 1, \tag{19}$$

where ν is the frequency of the light wave.

We define a function $E(z)$, such that $H(z) = E(z)H_0$:

$$E(z) = \sqrt{\Omega_{\text{m}}(1+z)^3 + \Omega_{\text{k}}(1+z)^2 + \Omega_{\Lambda}}, \tag{20}$$

where Ω_{m}, Ω_{k}, and Ω_{Λ} are the dimensionless density parameters that determine the dynamics of the Universe:

- Ω_{m} characterises the mass density of ordinary matter as well as dark matter:

  $$\Omega_{\text{m}} = \frac{8\pi G\rho_0}{3H_0^2}, \tag{21}$$

  where G is the gravitational constant and ρ_0 is the present-day matter density in the Universe.

- Ω_{Λ} measures the effective mass density of dark energy:

  $$\Omega_{\Lambda} = \frac{\Lambda c}{3H_0^2}, \tag{22}$$

  where Λ denotes the cosmological constant.

- Ω_k measures the curvature of space and is defined such that:

  $$\Omega_{\text{m}} + \Omega_{\Lambda} + \Omega_{\text{k}} = 1. \tag{23}$$

  In this work, we adopt a flat ΛCDM spacetime with $\Omega_{\text{k}} = 0$.

Hubble Distance

We can define a distance based on the Hubble flow, such that:

$$D_{\mathrm{H}} = \frac{c}{H_0}. \tag{24}$$

Comoving Distance

The comoving distance D_{C} between two close objects will remain constant with epoch if the objects movement follow the Hubble flow. The transverse comoving distance is the distance between two objects that are separated by an angle on the sky.

For $\Omega_{\mathrm{k}} = 0$, the transverse comoving distance D_{M} is equal to the line-of-sight comoving distance D_{C}:

$$D_{\mathrm{M}} = D_{\mathrm{C}} = D_{\mathrm{H}} \int_0^z \frac{\mathrm{d}z}{E(z)}. \tag{25}$$

Angular Diameter Distance

The angular diameter distance D_{A} of an object is defined as the ratio of its physical transverse size to its angular size.

$$D_{\mathrm{A}} = \frac{D_{\mathrm{M}}}{1+z}. \tag{26}$$

The angular diameter distance differs from the previously mentioned distances as it does not increase with z, but the more distant an object, the larger will be its angular size.

2.5 Gravitational Lensing

Gravitational lensing has the last decades become a favourable tool for studying cosmology. The notion that gravity affects light is by no means a new idea though. Various physicists, including Newton and Laplace, have since the eighteenth century proposed ways that mass could deflect light rays.

Albert Einstein realised it as a consequence of the principle of equivalence: that gravity and acceleration are not distinguishable. It is famously introduced by his elevator thought experiment. Inside an elevator, it is impossible to conduct an experiment that would indicate whether the elevator is standing still in a gravitational field or uniformly accelerating upwards. If a laser beam is shot horizontally from one side of the accelerating elevator to the parallel side, a person

inside the elevator will perceive the laser beam as curving downward. As there is no way to know if an elevator is accelerating or within a gravitational field, since the same must apply within a gravitational field, the consequence is that mass results in a gravitational field that must bend the path of light rays.

Einstein's Theory of General Relativity provides a full set of equations that describe this phenomenon. Light will always follow a null geodesic and travel the shortest distance between two points. In a flat spacetime, this will be a straight line. Another consequence of General Relativity is how mass bends spacetime. The stronger the gravity, the more spacetime is curved. In a curved spacetime, null geodesics will be curved too and the path of light rays will be bent.

The deflection angle of a ray of light is derived from general relativity:

$$\alpha = \frac{4GM}{c^2 R}, \tag{27}$$

where c is the speed of light and M is the mass of the object that induces the lensing effect for a light ray travelling at a distance R. During a solar eclipse in 1919, Eddington and Dyson confirmed this relation by observing how light from stars near the sun was deflected.

This effect can be seen when observing the Universe via the light from many distinct sources that passes in the vicinity of massive objects on its way to Earth. The deflection of light rays that are close to each other can be different, and will result in an object being distorted. This can increase the size of the image, causing it to appear larger. In other words, the massive object works as a magnifying lens.

It is possible to have multiple paths around the same lensing object and multiple images of the same source will appear. These paths will be of different lengths, corresponding to different travel times for the light. There is a gravitational time delay between the multiple sources.

This time delay is dependent on the mass of the lensing object and the redshift of the lens, and in some cases, the redshift of the source. It is purely a consequence of general relativity and is independent of cosmological assumptions. For this reason, it has become one of the preferred tools employed by researchers in many disciplines across astrophysics and cosmology (Congdon & Keeton, 2018).

2.5.1 Gravitational Time Delays

This section is based on equations in Congdon & Keeton (2018). When a light ray pass a massive objects, the total time delay is a sum of the gravitational time delay and the geometrical time delay.

$$\Delta t = t_{grav} + t_{geo} = \frac{(1+z_L)}{c}\frac{D_L D_S}{D_{LS}}\left(\frac{1}{2}(\overrightarrow{\theta} - \overrightarrow{\beta})^2 - \psi(\overrightarrow{\xi})\right) \tag{28}$$

where θ is the separation between images, β is the angular impact parameter and ψ is the lensing potential. The lensing potential will have a different form for different types of lensing object e.g. a Schwarzschild lens of a point mass or a singular isothermal sphere. The geometrical time delay is caused by the change in the geometrical path and the gravitational time delay is the Shapiro time delay (Shapiro, 1964) caused by gravitational time dilation.

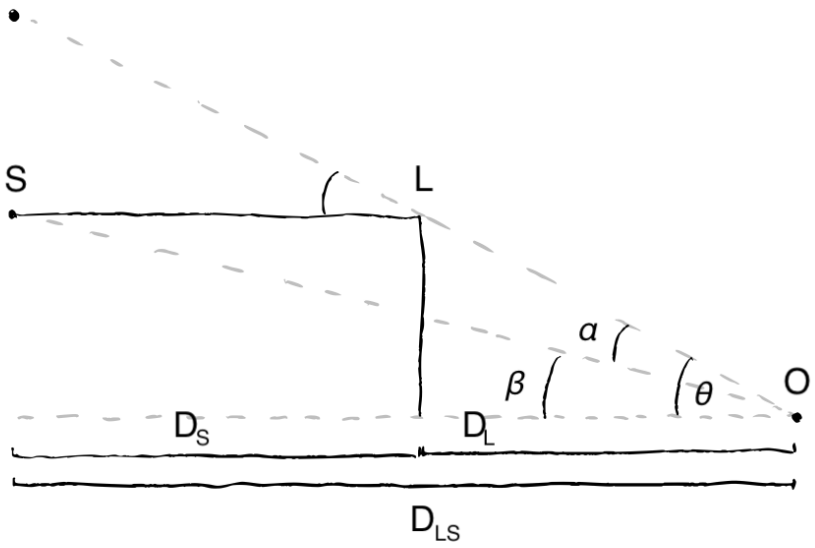

Figure 7: Drawn illustration of a gravitational lens.

Point mass

The simplest form of a lens is that of a single point mass. Compact objects, such as black holes, including primordial black holes, can be approximated as point mass lenses. The deflection angle of a point mass lens is:

$$\alpha = \frac{D_{\rm LS}}{D_{\rm L} D_{\rm S}} \frac{4GM_{\rm L}}{c^2 \theta}, \tag{29}$$

where $M_{\rm L}$ corresponds to the mass of the lensing object, with the angular diameter distances to the lens $D_{\rm L}$, to the source $D_{\rm S}$, and between the lens and source $D_{\rm LS}$.

This results in the angular Einstein radius:

$$\theta_{\rm E} = 2\sqrt{\frac{GM_{\rm L}}{c^2} \frac{D_{\rm LS}}{D_{\rm L} D_{\rm S}}}. \tag{30}$$

The lens equation then takes the form:

$$\beta = \theta - \frac{\theta_{\rm E}^2}{\theta}, \tag{31}$$

where β is the angular impact parameter. From this, we can define the normalised impact parameter as

$$y = \beta / \theta_{\rm E}. \tag{32}$$

A point mass will produce two images with the positions:

$$\theta_{\pm} = \frac{1}{2}(\beta \pm \sqrt{\beta^2 + 4\theta_{\rm E}^2}). \tag{33}$$

One image will be formed on the same side as the source, and another will be formed on the opposite side. The image on the same side as the source will have the largest magnification. The magnifications are given by:

$$\mu_{\pm} = \frac{1}{2} \pm \frac{y^2 + 2}{2y + \sqrt{y^2 + 4}}, \tag{34}$$

with the flux ratio between the images being:

$$R_{\rm f} = \left| \frac{\mu_+}{\mu_-} \right| = \frac{y^2 + 2 + y\sqrt{y^2 + 4}}{y^2 + 2 - y\sqrt{y^2 + 4}}. \tag{35}$$

The flux ratio constrains the impact parameter y to be smaller than:

$$y_{\rm max} = \left(\frac{1 + \bar{R}_{\rm f}}{\sqrt{\bar{R}_{\rm f}} - 2} \right)^{\frac{1}{2}} \tag{36}$$

From combining the above equations, we find that the time delay between the two images is determined by the lens mass, lens redshift, and the normalised impact parameter, as follows:

$$\Delta t = \frac{4GM_{\rm L}}{c^3}(1 + z_{\rm L}) \left[\frac{y}{2}\sqrt{y^2 + 4} + \left(\frac{\sqrt{y^2 + 4} + 4}{\sqrt{y^2 + 4} - 4} \right) \right]. \tag{37}$$

Single Isothermal Sphere

Dark matter halos can consist of both cold dark matter as well as warm dark matter. These halos behave as an ideal gas in a spherically symmetric gravitational potential. This means that such halos can be parametrised with the profile of a singular isothermal sphere (SIS).

A SIS will produce two images if the source lies within the Einstein ring, if $\beta < \theta_{\rm E}$:

$$\theta_{\rm E} = 4\pi \frac{v^2}{c^2} \frac{D_{\rm LS}}{D_{\rm S}}. \tag{38}$$

The lens equation takes the form:

$$\theta_{\pm} = \beta \pm \theta_{\rm E}. \tag{39}$$

The magnification of the images as a function of image position is given by:

$$\mu = \frac{|x|}{|x| - 1}. \tag{40}$$

with $x = \theta/\theta_{\rm E}$. For a source located within the Einstein radius there are two solutions: $x = y+1$ and $x = y - 1$.

The flux ratio between two images is given by:

$$R_{\rm f} = \left| \frac{\mu_+}{\mu_-} \right| \tag{41}$$

The maximum flux ratio $R_{\rm f} < \bar{R}_{\rm f}$ constrains the impact parameter y to be smaller than:

$$y_{\rm max} = \frac{R_{\rm f} - 1 - \sqrt{9R_{\rm f}^2 - 10R_{\rm f} + 1}}{2R_{\rm f} - 2}. \tag{42}$$

The time delay between two images is then:

$$\Delta t = 16\pi^2 \frac{v^4}{c^5} \frac{D_{\rm L} D_{\rm LS}}{D_{\rm S}} (1 + z_{\rm L}) 2y, \tag{43}$$

where v is the velocity dispersion. If the system is in virial equilibrium ($2T = U$), velocity dispersion can be related to mass as:

$$2v^2 = \frac{GM}{R}. \tag{44}$$

The radius of an isothermal sphere can be related to mass and density via the definition of the virial mass. We use the convention where the overdensity constant is $\Delta_c = 200$ (White, 2001), and it follows that:

$$\Delta_c \cdot \rho_c = \frac{M_{200c}}{\frac{4}{3}\pi R_{200c}^3}. \tag{45}$$

The velocity is then defined from the mass, such that:

$$v = \left[\frac{100}{3} G^3 M^2 \pi \rho_{\rm c}\right]^{\frac{1}{6}}, \tag{46}$$

with

$$\rho_{\rm c} = \frac{3H^2(z)}{8\pi G}. \tag{47}$$

2.5.2 Lensing Probability

The integrated optical depth is related to the lensing probability as:

$$P = 1 - e^{\bar{\tau}} \approx \bar{\tau}, \tag{48}$$

where $\bar{\tau}$ is the integrated optical depth over all redshifts.

This implies that if we have N FRBs, we expect that the number of lensed FRBs will be:

$$N_{\rm lensed} = N_{\rm FRB}\bar{\tau}. \tag{49}$$

The integrated optical depth can be calculated as (Muñoz et al., 2016):

$$\bar{\tau}(M_{\rm L}) = \int {\rm d}z\, \tau(z, M_{\rm L}) N(z), \tag{50}$$

where $N(z)$ is the redshift distribution of FRBs (see Section 3.1).

The optical depth of a source at $z_{\rm S}$ is given as:

$$\tau(M_{\rm L}, z_{\rm S}) = \int_0^{z_{\rm S}} {\rm d}\chi(z_{\rm L})(1+z_{\rm L})^2 n_L \sigma(M_{\rm L}, z_{\rm L}), \tag{51}$$

where $\chi(z_{\rm L})$ is the comoving distance at $z_{\rm L}$ and $n_{\rm L}$ is comoving number density of lenses. σ is the lensing cross section given by:

$$\sigma(M_{\rm L}, z_{\rm L}) = \pi\theta_{\rm E}^2 D_{\rm L}^2 \left[y_{\rm max}^2 - y_{\rm min}^2(M_{\rm L}, z_{\rm L})\right]. \tag{52}$$

In the case of PBHs:

$$\sigma(M_{\rm L}, z_{\rm L}) = \frac{4\pi G M_{\rm L}}{c^2} \frac{D_{\rm L} D_{\rm LS}}{D_{\rm S}} \left[y^2_{\rm max} - y^2_{\rm min}(M_{\rm L}, z_{\rm L}) \right] . \tag{53}$$

$$\tau(M_{\rm L}, z_{\rm S}) = \frac{3}{2} f_{\rm DM} \Omega_{\rm c} \int_0^{z_{\rm S}} {\rm d}z_{\rm L} \, \frac{H_0^2}{cH(z_{\rm L})} \frac{D_{\rm L} D_{\rm LS}}{D_{\rm S}} (1+z_{\rm L})^2 \left[y^2_{\rm max} - y^2_{\rm min}(M_{\rm L}, z_{\rm L}) \right] , \tag{54}$$

where $f_{\rm DM}$ is the fraction of dark matter that is in this form, and $\Omega_{\rm c}$ is the dark matter density today (Muñoz et al., 2016).

In the case of Dark Matter Halos:

$$\sigma(M_{\rm L}, z_{\rm L}) = 16\pi^3 \frac{v^4}{c^4} \left(\frac{D_{\rm L} D_{\rm LS}}{D_{\rm S}} \right)^2 \left[y^2_{\rm max} - y^2_{\rm min}(M_{\rm L}, z_{\rm L}) \right] . \tag{55}$$

For dark matter halo, the distribution of halos is described by the HMF: $\frac{{\rm d}n}{{\rm d}\ln M_{\rm L}}$.

We can define $\frac{{\rm d}\tau(M_{\rm L}, z_{\rm S})}{{\rm d}\ln M_{\rm L}}$ by replacing the comoving number density $n_{\rm L}$ in Equation (51) with the HMF, as follows:

$$\frac{{\rm d}\tau(M_{\rm L}, z_{\rm S})}{{\rm d}\ln M_{\rm L}} = 16\pi^3 \left(\frac{25}{2} \right)^{\frac{2}{3}} (G M_{\rm L})^{\frac{4}{3}} \int_0^{z_{\rm S}} \frac{{\rm d}n}{{\rm d}\ln M_{\rm L}} {\rm d}z_{\rm L} \frac{H(z)^{\frac{1}{3}}}{c^3} \left(\frac{D_{\rm L} D_{\rm LS}}{D_{\rm S}} \right)^2 (1+z_{\rm L})^2 \left[y^2_{\rm max} - y^2_{\rm min}(M_{\rm L}, z_{\rm L}) \right] . \tag{56}$$

2.6 Fast Radio Bursts

The existence of fast radio bursts (FRBs) is a fairly new discovery, with the first FRB being discovered in 2007 by the Parkes telescope (Lorimer et al., 2007). It was a strange object with a brightness at about 30 jansky, while it seemed to have originated billion pc away. The burst was unlike anything that had previously been observed. A powerful transient that came from far away in the universe presented endless opportunities.

In 2013, four similar radio transients were discovered. Since then, more than a hundred of FRBs have been observed. Some were found by going through old data and many more are being detected by experiments that are particularly designed for FRB detection. FRBs are still of unknown origin, though the data suggests that they are at least of cosmological nature. In 2016, it was discovered that a small fraction of FRBs are repeating. Repeating FRBs seem to occur on different scales from around a day to a year (Petroff et al., 2021). Most repeaters repeat multiple times.

So far, FRBs have only been detected in radio frequencies between 400 MHz and 8 GHz, with no counterpart in other parts of the electromagnetic spectrum. Until 2020, the pulse durations of most FRBs have been found in the range of 10^{-1} to 10^{1} ms (Petroff et al., 2019). The FRB with the smallest pulse duration detected at the start of thesis was FRB 121102, with a duration of merely 30 μs. More recent studies have also achieved a temporal resolution of FRBs on the order of 10 μs (Sammons et al., 2020).

More than 50 different progenitor theories of FRBs have been published. The majority of these theories involve some version of neutron stars. Neutron stars have large rotational energies and strong magnetic fields. Presently, the most popular theory is that FRBs are produced by magnetars (Petroff et al., 2021).

2.6.1 Dispersion Measure

When electromagnetic waves propagate through a medium of cold plasma, they will experience a dispersion - a change in group velocity which depends on frequency. The plasma works as a refractive index (Lorimer & Kramer, 2012):

$$\delta t \propto DM \cdot \nu^{-2} \tag{57}$$

where DM is the the dispersion measure (DM). The proportionality to ν^{-2} makes this effect particularly interesting when considering radio waves.

The DM is the integrated electron column density along the line of sight and is measured in cm^{-3} pc:

$$DM = \int_0^d n_e(l)\mathrm{d}l, \tag{58}$$

where n_e is the electron density and d is the distance to the source.

The observed dispersion measure of an FRB is the total integrated electron density from the source to the observer, and is made up of components from the Milky Way, the host galaxy and the intergalactic medium (IGM):

$$DM_{\mathrm{obs}} = DM_{\mathrm{MW}} + DM_{\mathrm{host}} + DM_{\mathrm{IGM}}. \tag{59}$$

Most FRBs have an observed dispersion measure between 500–1000 cm^{-3} pc which suggests that they are of extragalactic origin.

$DM_{\rm MW}$ and $DM_{\rm host}$

$DM_{\rm MW}$ and $DM_{\rm host}$ can vary greatly depending on where the FRB is observed on the sky and where it is located in the host galaxy. $DM_{\rm MW}$ can be inferred from different models whereas $DM_{\rm host}$ as of now is unfeasible to estimate and can vary anywhere from 20–500 pc cm^{-3} e.g. if it is in a galaxy similar to the Milky Way (Murray et al., 2013b). So far, there are only 19 FRBs with an identified host galaxy (Heintz et al., 2020) and even in these cases, we cannot adequately measure the $DM_{\rm host}$. Typically, one either makes an average guess similar to the type of galaxy that has been identified or use a maximum $DM_{\rm IGM}$, which will ultimately correspond to a maximum redshift.

$DM_{\rm IGM}$

The redshift of an FRB can be calculated from an estimate of the electron density of the intergalactic medium (IGM). The approximation listed in the `FRBcat` catalogue has the following form:

$$z = \frac{DM_{\rm IGM}}{1200 \text{ pc cm}^{-3}} \tag{60}$$

for lower redshifts (Petroff et al., 2016).

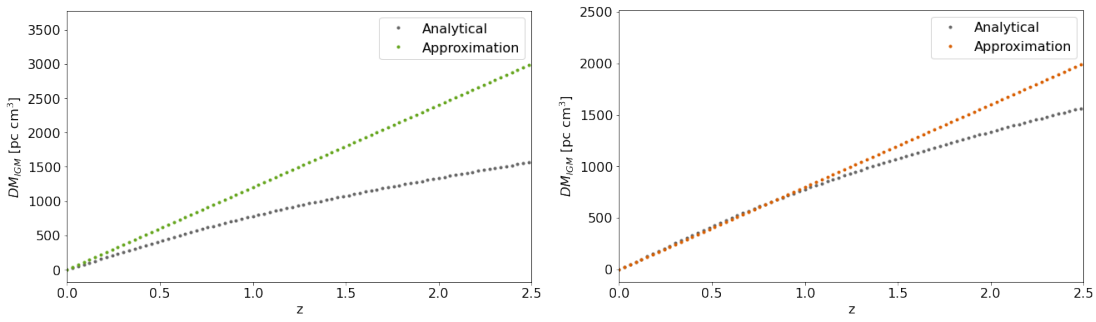

(a) (b)

Figure 8: Comparison of the approximation and analytical functions with a proportionality constant of (a) 1200 pc cm^{-3}, and (b) 800 pc cm^{-3}.

We test different assumptions and divide with numbers from 700–1200 pc cm^{-3}. We plot the residuals between the approximations and the analytic function (Deng & Zhang, 2014), and compare the results in Figure 9. For redshifts up to $z = 1$, the approximation is most adequate when we divide by 800 pc cm^{-3}.

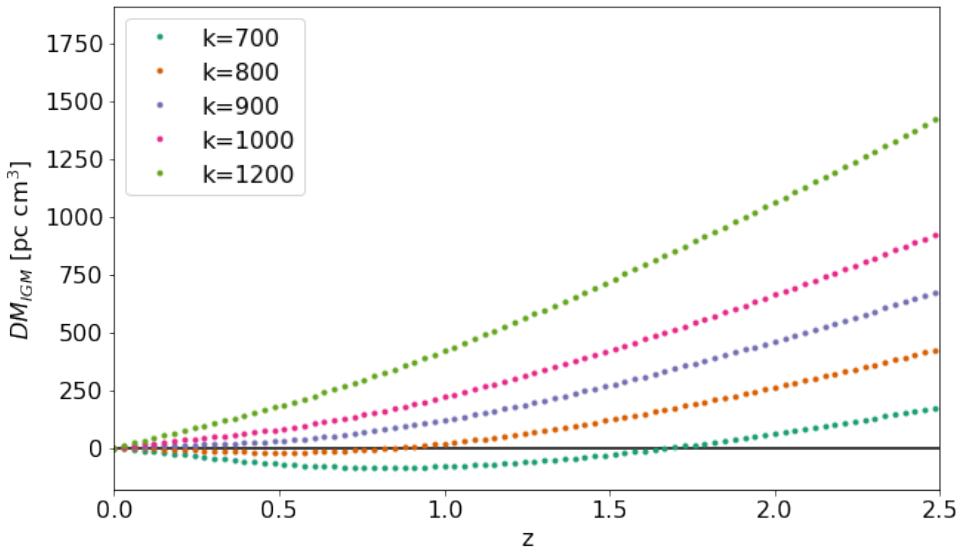

Figure 9: Residuals of the approximations and the analytical function. The approximation with k = pc cm^{-3} provides the best assumption.

2.6.2 Plasma Lensing

Similar to the effect seen in dispersion measure, when electron density in plasma affects electromagnetic waves, a concentrated density of electrons can cause refractive deflections of light waves and work similarly to a lens. This effect is known as plasma lensing.

Contrary to the effects of gravitational lensing, plasma lensing will affect the electromagnetic waves chromatically such that lower frequencies will have a larger time delay, just as we see with dispersion measure. For radio waves, such as FRBs, this effect might not be negligible.

Similarly to gravitational lensing, the plasma lensing time delay is a sum of the geometrical and the plasma time delay (Wagner & Er, 2020), with the plasma potential given as:

$$\psi_{\text{plasma}}(x) = -\frac{D_{\text{LS}}}{D_{\text{L}} D_{\text{S}}} \frac{r_e \lambda^2}{2\pi} N_e(x), \tag{61}$$

where r_e is the classical electron radius, λ is the wavelength and $N_e(x)$ is the integrated electron density along the line of sight, i.e. the dispersion measure.

2.6.3 Experiments

As of the start of this thesis, there were 110 FRB detections listed in the `FRBcat`. Multiple experiments are actively searching for FRBs, with CHIME, Parkes and ASKAP accounting for

most of the detections. At the time of writing, CHIME is detecting on the order of 10 FRBs every day, so these numbers are rapidly increasing.

Parkes is a historical, single dish radio telescope with a size of 64 m in New South Wales, Australia. The telescope consists of 13 beams that cover a sky area of 0.5 deg^2. It has a bandwidth at 400 MHz and a 0.064 ms temporal resolution, making it an ideal telescope for FRB detection. It has a high sensitivity with a limiting signal to noise ratio (S/N) of 16, resulting in the possibility of finding FRBs at high redshift (Petroff et al., 2015).

Figure 10: Photo of the ASKAP telescope. Credit: CSIRO

The Australian Square Kilometre Array Pathfinder (ASKAP) telescope is located in the desert of Western Australia. ASKAP consists of 36 12-m dish antennas and cover a sky area of 30 deg^2 (Macquart et al., 2010). Each antenna can be pointed in independent directions of the sky and take the "Fly's Eye" configuration, which allow them to cover up to 160 deg^2 (Bannister et al., 2017). ASKAP will only detect the brightest FRBs and, hence, it has the lowest measures of dispersion measure (James et al., 2019). However, with ASKAP, it is possible to identify the host galaxy of FRBs, as the telescope can localise FRBs to $< 1''$ (Heintz et al., 2020). Another advantage of ASKAP is its high time resolution, making it possible to resolve FRB temporal features on a 10 μs scale (Sammons et al., 2020).

The Canadian Hydrogen Intensity Mapping Experiment (CHIME) in British Columbia was, as the name suggests, originally designed for hydrogen intensity mapping, but has become one of the leading FRB experiments with a detection rate of around 10 FRBs per day. CHIME is made up of four semi-cylindrical parabolic reflectors with a size of 20 m x 100 m each, thereby resulting in a large field view of $\sim$ 200 square degrees. CHIME's frequency range of 400–800

Figure 11: Photo of the CHIME telescope. Credit: McGill University

MHz and its temporal resolution of 0.983 ms makes it an ideal telescope for searching for FRBs (CHIME/FRB Collaboration et al., 2018).

In the recently published CHIME/FRB catalogue (CHIME/FRB Collaboration et al., 2021), more than 600 new FRBs, including many repeaters, were added to the catalogue, and CHIME is now without a doubt the leading experiment for FRB detection in numbers.

The particular nature of FRBs and their short time scale make lensed FRBs an exceptional probe for detecting dark matter. Especially for dark matter in the form of PBHs, the ms scale corresponds to the mass window of 20 to 100 $M_\odot$ where PBH dark matter can exist. In the case of CDM and WDM in dark matter halos, the HMF predicts a difference in the number of halos for different particle masses. This difference is distinctive on the mass scales that corresponds to time delays on ms scale.

In the following section, we will go through calculations of potentially lensed FRBs for dark matter in the case of PBHs, CDM, and WDM.

3 Lensed FRBs

For the computations described in this thesis, we use the python package `astropy` for the physical constants and to calculate the cosmological parameters and distances.

3.1 Redshift Distribution

The lensing probability is dependent on the redshift distribution of the FRBs. As we go to higher redshift, there is a higher probability of an intervening lens object between the source and the observer.

FRB data is available through the online catalogue `FRBcat` (Petroff et al., 2016). The catalogue contains FRBs from diferent surveys with Parkes, CHIME, ASKAP and UTMOST producing most of the observations.

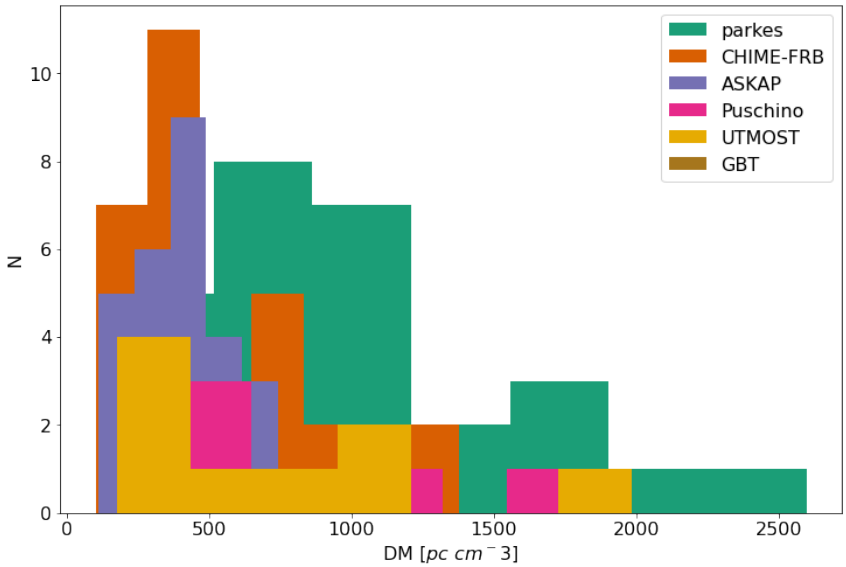

Figure 12: Histogram of all FRB DM_{excess} available in FRBCAT.

Listed in the catalogue among others is the telescope name, DM, DM_{excess}, redshift z, as well as RA and DEC. DM_{excess} is found by subtracting the Milky Way contribution M_{MW} using the NE2001 Galactic electron density model (Cordes, 2004). The redshift is estimated without subtracting the dispersion measure contribution from the host galaxy DM_{host} but simply applying the DM - z approximation: $z = DM_{\text{excess}}/1200$ pc cm^{-3}. The total dispersion measure in the `FRBcat` catalogue is calculated using fit models described in Thornton et al. (2013).

In Figure 12, we illustrate the histogram of the excess dispersion measure from the FRBcat catalogue. Equation (60) can be used to estimate the redshifts from dispersion measures with the proportionality constant as 800 pc cm^{-3}.

In Figure 13, we depict the histograms of the redshifts for each of the surveys Parkes, CHIME, ASKAP and UTMOST, and fit them to two possible redshift distributions. The first one has a constant comoving density, while the second one follows the star formation history (Muñoz et al., 2016):

$$N_{\text{constant}}(z) = \mathcal{N}\frac{\chi^2(z)}{H(z)(1+z)}e^{\frac{-d_{\text{L}}^2(z)}{2d_{\text{L}}^2(z_{\text{cut}})}} \tag{62}$$

$$N_{\text{SFH}}(z) = \mathcal{N}\frac{\dot{\rho}_*(z)\chi^2(z)}{H(z)(1+z)}e^{\frac{-d_{\text{L}}^2(z)}{2d_{\text{L}}^2(z_{\text{cut}})}} \tag{63}$$

$$\dot{\rho}_*(z) = h\frac{a+bz}{1+(\frac{z}{k})^d}, \tag{64}$$

where $a = 0.0170$, $b = 0.13$, $k = 3.3$, $d = 5.3$, and $h = 0.7$ (Caleb et al., 2016).

We fit the distributions with the normalisation $\mathcal{N}$ and the cut-off redshift z_{cut} as the fitting parameters. z_{cut} is a Gaussian cut off related to the telescope sensitivity and will vary for different experiments. The fits are performed using χ^2-regression. All fits converge and have reasonable χ^2-probabilities between 0.1 and 0.9.

For both distributions, the cut-off redshift is dependent on the survey and the sensitivity of the detector. Parkes has the highest redshift cut-off of $z_{\text{cut}} = 0.8$ (cf. Figure 13b). To be able to compare the results easily to the paper by Muñoz et al. (2016), we adopt a similar normalised redshift distribution that describes the first 17 detections with redshift from the FRB catalogue with redshift cut-off at $z_{\text{cut}} = 0.5$ (cf. Figure 13a). The excess dispersion measure from FRBcat have not had DM_{host} subtracted, so the redshifts should be considered as maximum redshifts. As an example, FRB 121102 is included with $z = 0.31$, but has since had its host identified to a dwarf galaxies at $z = 0.19273(8)$ (Tendulkar et al., 2017).

From the recently released CHIME-FRB catalogue containing more than 500 FRBs, we obtain a more accurate distribution of the possible CHIME detections. For a more reasonable redshift distribution, we asumme as host DM more or less like the Milky Way with DM_{host} = 100 pc cm^{-3} and subtract it from the DM_{excess} before computing the redshift. Just as in the case of the FRBcat, DM_{excess} is estimated from the NE2001 model (Cordes, 2004). The redshift is then estimated using Equation (60) but with 800 pc cm^{-3} as the proportionality constant. We

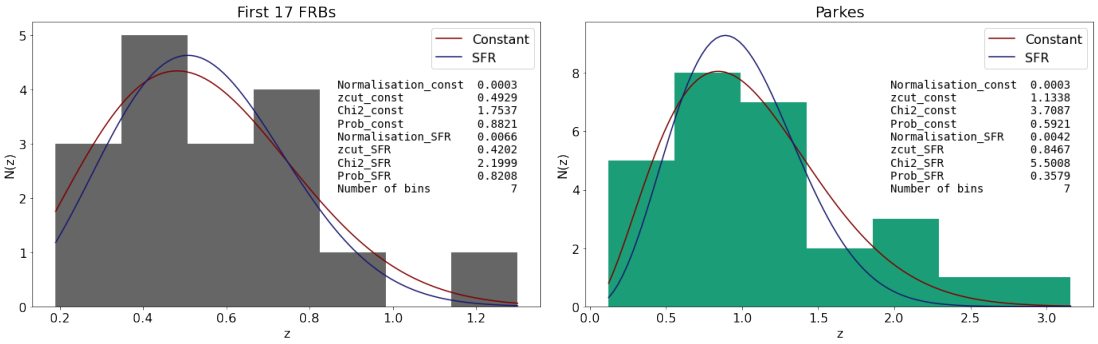

(a)

(b)

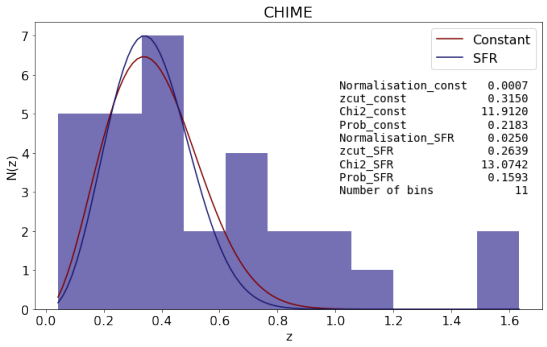

(c)

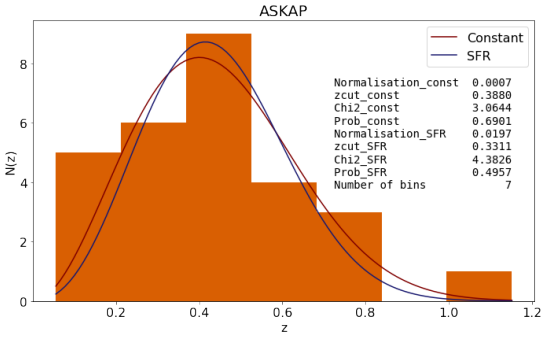

(d)

Figure 13: Redshift distribution fits with (a) $z_{\rm cut} = 0.5$, (b) $z_{\rm cut} = 0.8$, (c) $z_{\rm cut} = 0.25$, and (d) $z_{\rm cut} = 0.35$.

fit this distribution and find that it actually looks very similar to the first 17 detected FRBs and the distribution that is applied by Muñoz et al. (2016) with a $z_{\rm cut} \sim 0.5$ (cf. Figure 14). Since CHIME will likely dominate the next series of FRB detections, a distribution with $z_{\rm cut}$ = 0.5 constitutes a reasonable choice.

3.2 Time Delays

The different lensing potentials of the point mass and SIS models result in different time delays for the same mass. This means that an SIS lens with a higher mass can have a similar time delay to a point mass lens with a smaller mass. A minimum time delay of $\Delta t = 1$ ms corresponds to different mass scales for different lenses. For a typical situation with $z_{\rm S} = 1$, $z_{\rm L} = 0.5$ and $y = 0.2$, we see that lensed FRBs can be observed if they are lensed by a point mass lens with $M_{\rm L} > 10 M_{\odot}$ and an SIS lens with $M_{\rm L} > 10^5 M_{\odot}$ (cf. Figure 15).

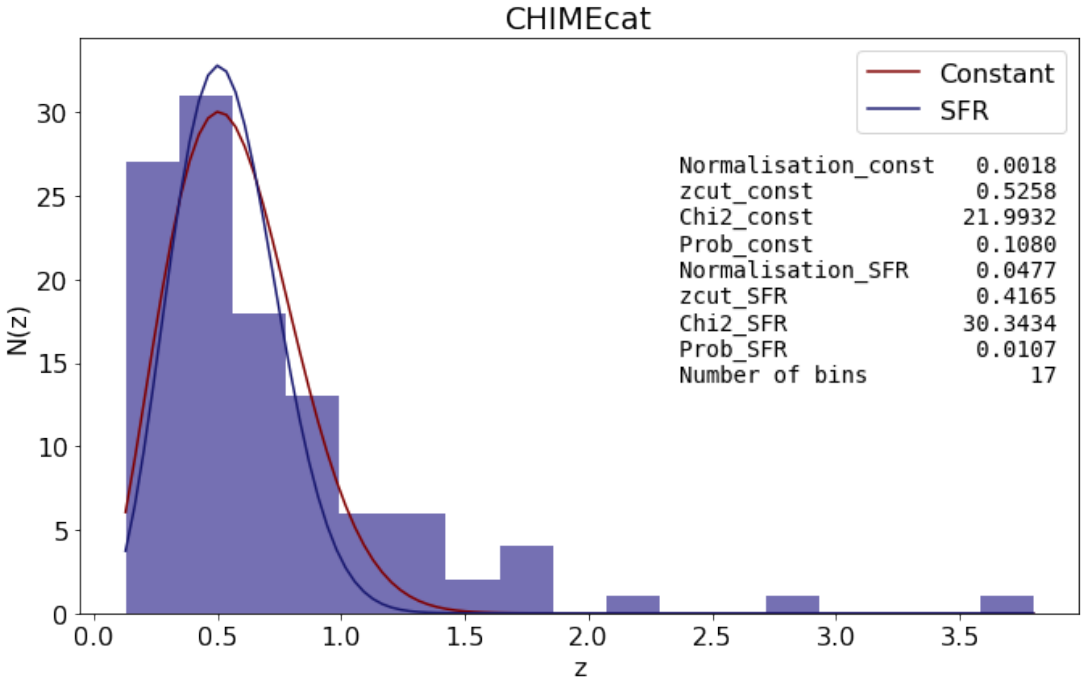

Figure 14: Redshift distribution fit for the 2021 CHIME/FRB catalogue data.

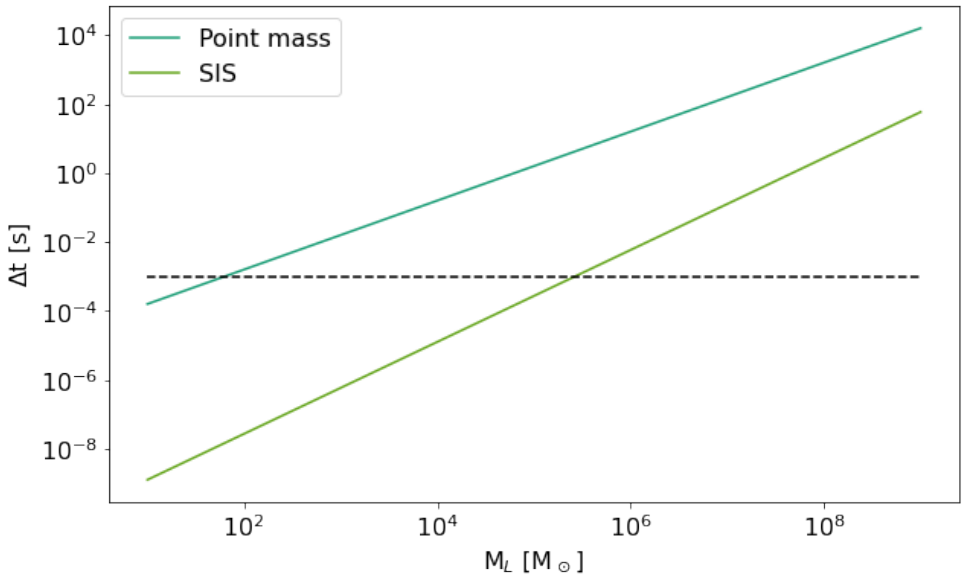

Figure 15: Typical gravitational time delays Δt for the point mass and SIS lens models. The dashed line indicates where Δt crosses 1 ms for a scenario with $z_{\rm S} = 1$, $z_{\rm L} = 0.5$ and $y = 0.2$,.

3.3 Lensing of Primordial Black Hole

We assume that if dark matter is made up of PBHs, the mass function will be a delta function with mass between 20–200 $M_\odot$. As such, in this simplified model, PBHs will consist of only

one mass type.

$y_{\rm min}$ will correspond to the minimum time delay of $\Delta t = 0.01$, 0.3, 1 and 3 ms, respectively.These time delays correspond to the characteristic duration of an FRB as well as what different surveys can resolve. $y_{\rm min}$ will depend on the mass of the lens objects $M_{\rm L}$ and the redshift of the lens $z_{\rm L}$. $y_{\rm max}$ can be found from Equation (36) and we set $\bar{R}_{\rm f} = 5$ so that both images are detectable.

We calculate the integrated optical depth $\bar{\tau}$ for the four minimum time delays $\Delta t = 0.01, 0.3, 1, 3$ ms, and for both FRB redshifts distributions $N_{\rm constant}(z)$ (see Equation (62)) and $N_{\rm SFH}(z)$ (see Equation (63)) with $z_{\rm cut} = 0.5$.

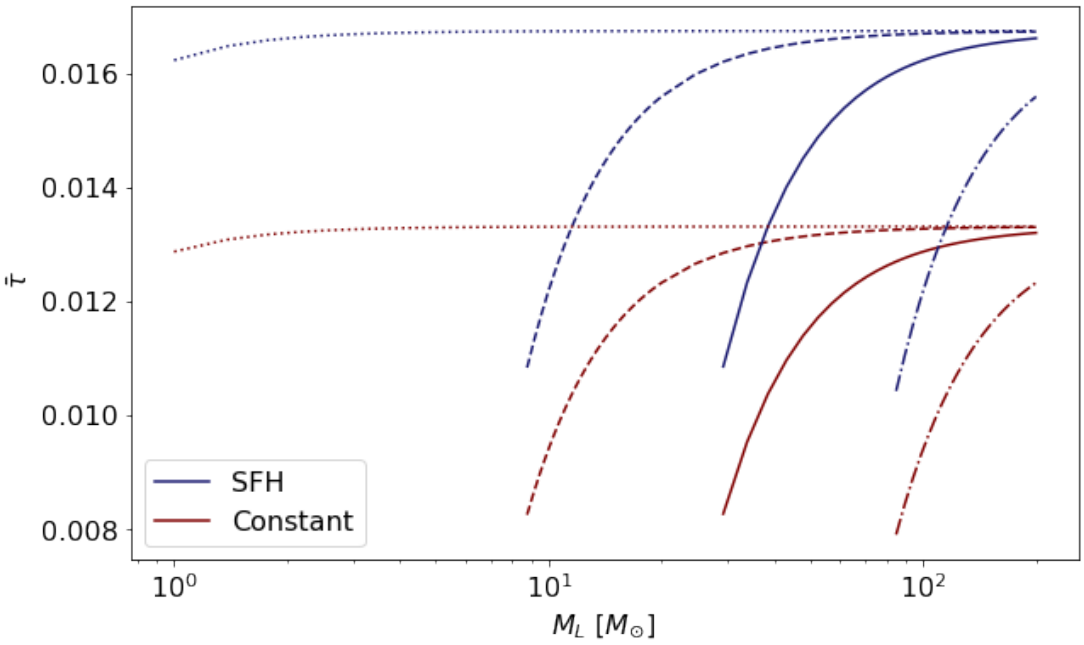

Figure 16: Integrated optical depth for a population of FRBs with a constant comoving density (red line) and a population that follows SFH (blue line) for a minimum time delay of 0.01 (dotted), 0.3 (dashed), 1 (solid) and 3 ms (dot-dashed), respectively.

A redshift distribution that follows star formation history results in a higher integrated optical depth $\bar{\tau}$ than one with a constant comoving density as it leads to higher redshifts for a given distribution of FRBs.

Since the number of lensed FRBs is equal to $N = N_{\rm FRB}\bar{\tau}$, we can find the minimum fraction $f_{\rm DM}$ of dark matter that will result in only 1 lensed FRB out $N_{\rm FRB}$. As in the paper by Muñoz et al. (2016), we set the expected number of FRBs per year to an optimistic but yet realistic

number of $N_{\rm FRB} = 10^4$ (Connor et al., 2016), which yields $\bar{\tau} = 1/10^4$. It follows that:

$$\bar{\tau} \cdot f_{\rm DM} = \frac{1}{10^4}. \tag{65}$$

We illustrate this in Figure 17. If less than 1 out 10^4 FRBs are lensed, we can constrain the fraction of dark matter in the form of PBHs with $M_{\rm L} > 10$ $M_\odot$ to less than 0.6 per cent and 0.8 per cent for the different redshift distributions, respectively. A higher $z_{\rm cut}$ and larger number of FRBs will provide stronger constraints on the fraction of dark matter in the form of PBHs.

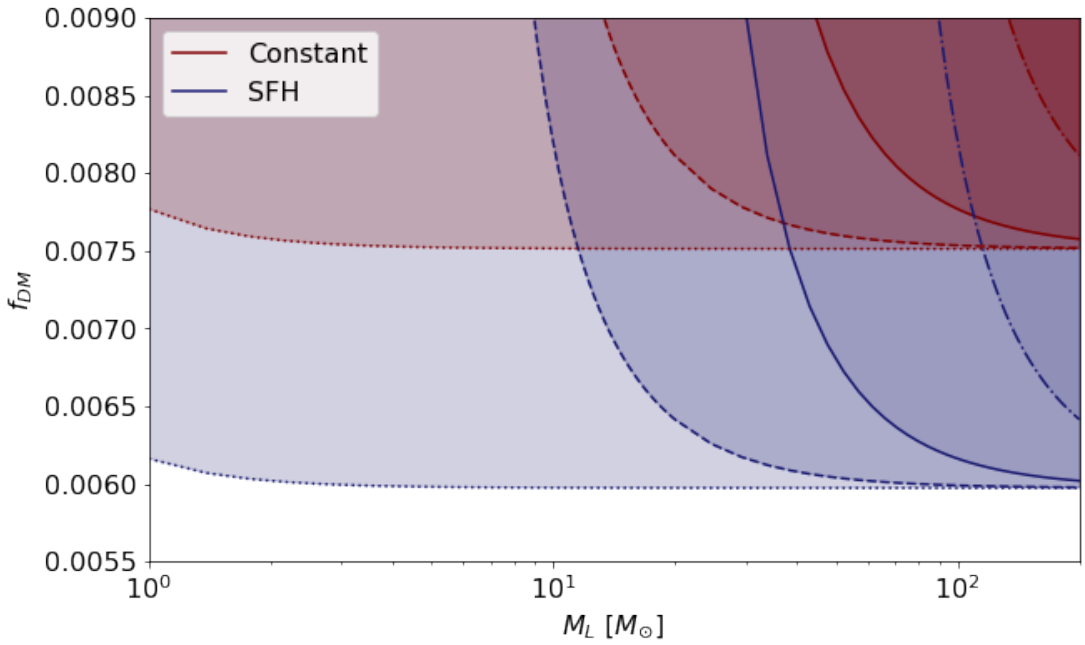

Figure 17: Expected upper bounds in $f_{\rm DM}$ from future observations of FRBs, expecting no detection of lensing in a sample of 10^4 FRBs. For a population of FRBs with a constant comoving density (red line) and a population that follows SFH (blue line) for a minimum time delay of 0.01 (dotted), 0.3 (dashed), 1 (solid) and 3 ms (dot-dashed), respectively.

3.3.1 Experiments and Different Redshift Distributions

From the `FRBcat` data with 110 detected FRBs, we see a clear difference in the redshift distribution of Parkes, CHIME and ASKAP. This will affect the final integrated optical depth $\bar{\tau}$. A difference in z_{cut} subsequently results in a large difference for the optical depth.

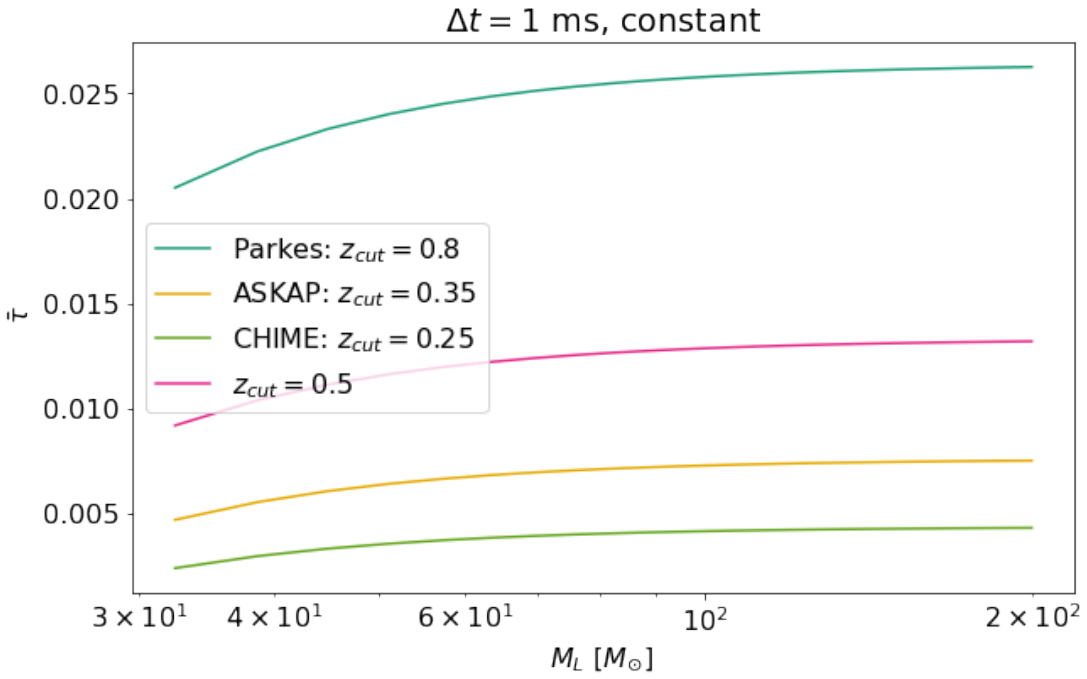

Figure 18: Integrated optical depth $\mathrm{d}\bar{\tau}$ for a population of FRBs with a constant comoving density for Parkes, ASKAP and CHIME data available in `FRBcat` for a minimum time delay of Δt = 1 ms.

CHIME FRB Catalogue 2021

The 599 FRBs detected in the CHIME FRB catalogue, released in June 2021, follow a redshift distribution with a cut-off redshift $z_{\rm cut}$ that is very similar to our optimistic assumptions based on the work by Muñoz et al. (2016).

Using this available data and Equation (49), if less than one out of the 599 detected FRBs are lensed, we can derive constraints on dark matter in the form of PBH.

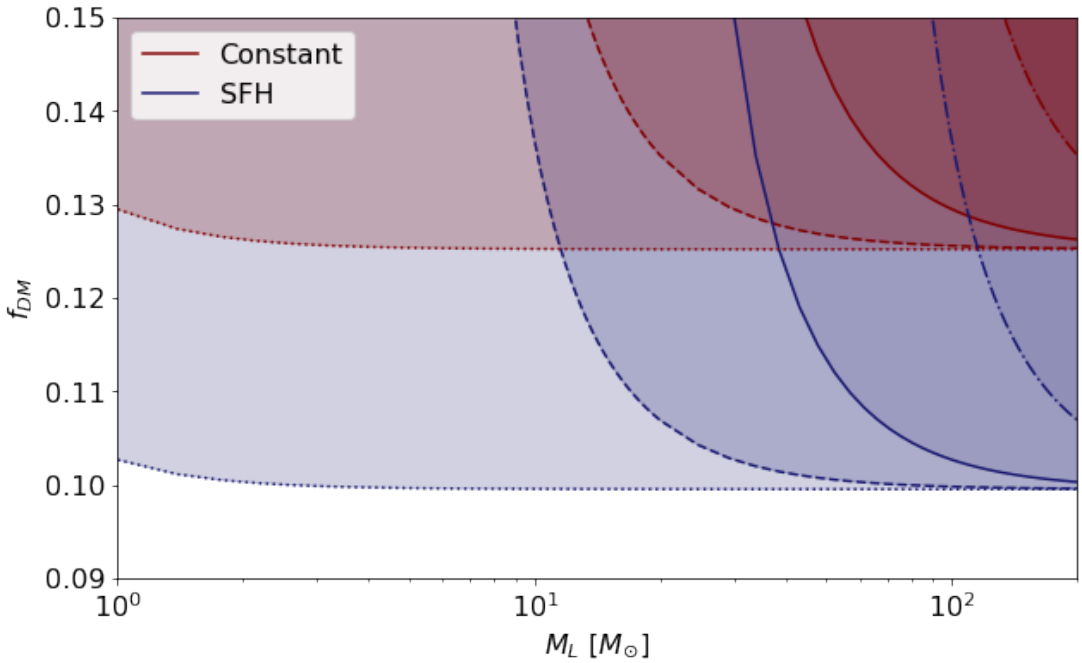

Figure 19: Constraints on the fraction of dark matter in the form of PBHs from a data sample of the size of the data in CHIME/FRB catalogue. For a population of FRBs with a constant comoving density (red line) and a population that follows SFH (blue line) for a minimum time delay of 0.01 (dotted), 0.3 (dashed), 1 (solid) and 3 ms (dot-dashed), respectively.

Consequently, with the currently available data, it is possible to constrain that dark matter in the form of PBHs with $M_{\rm L} > 10$ M$_\odot$ comprises less than 10% or 13% if none of the FRBs are lensed.

3.4 Lensing by a Dark Matter Halo

Similarly to the case of a point mass lens, we can calculate the optical depth for FRBs lensed by dark matter halos.

$y_{\rm min}$ will correspond to the minimum time delay that we set to $\Delta t = 1$ ms. This will depend on $M_{\rm L}$ and the angular diameter distances that depend on z. $y_{\rm max}$ is found from Equation (42) and we again choose $\bar{R}_{\rm f} = 5$. $\bar{\tau}$ is calculated for $N_{\rm constant}$ (Equation (62)) and $N_{\rm SFH}$ (Equation (63)), respectively.

For the halo mass function, we employ the halo mass function calculator for Python, as provided by `hmfcalc`, for both CDM and WDM. For the WDM scenario, we examine different cases of particle masses with m_x = 1, 2, 4 and 100 keV, respectively. We expect that the different particle masses will result in different optical depths, since the different HMF cut-off for each type of WDM is significant for halo with a mass of 10^5–10^{11} $M_\odot$.

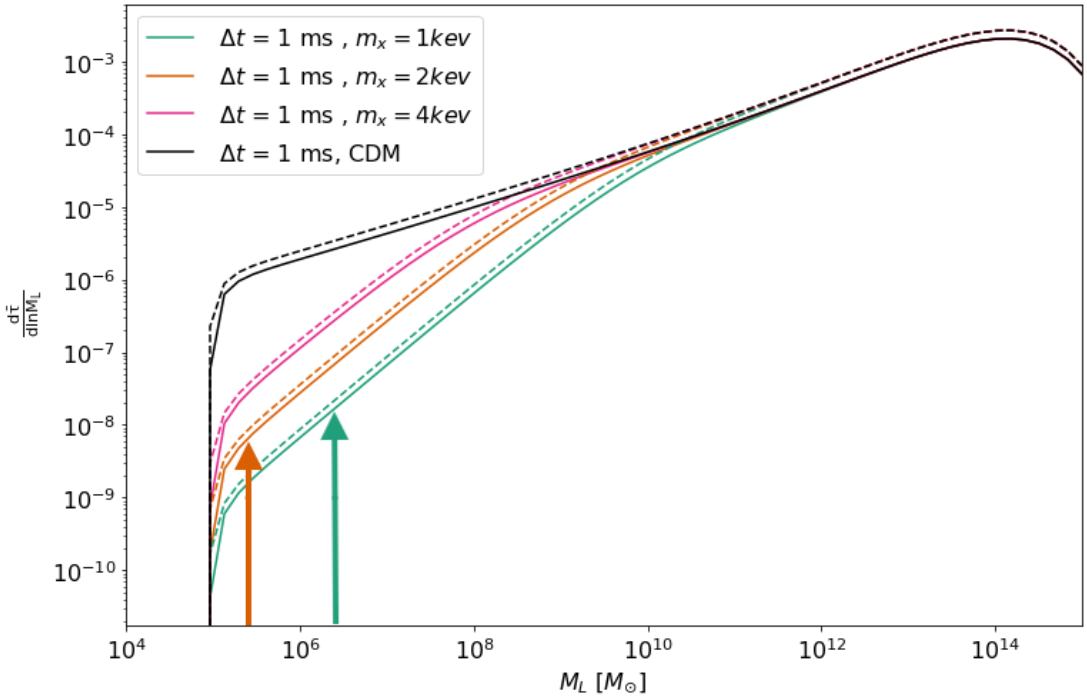

Figure 20: $\mathrm{d}\bar{\tau}/\mathrm{d}\ln M_L$ for a population of FRBs with a constant comoving density (solid) and a population that follows SFH (dashed). Computed for a minimum time delay of $\Delta t = 1$ ms. The arrows indicate the free streaming mass of the different WDM particles. Below these masses the optical depth is zero.

$\mathrm{d}\bar{\tau}/\mathrm{d}\ln M_L$ peaks around $M_{\rm L} = 10^{14}$ $M_\odot$. This will correspond to a time delay on the order of 1000 days for an arbitrary choice of $z_L = 0.5$ and $y = 0.2$. Since some FRBs are known to repeat, we want to choose a reasonable maximal time delay such that we do not easily confuse lensed FRBs with repeaters. As most repeaters recur after more than 24 hours, we consider $\mathrm{d}\bar{\tau}/\mathrm{d}\ln M_L$ below a maximum time delay at 24 hours which corresponds roughly to a halo

mass of $M_{\rm L} \sim 10^{11}$ M$_\odot$.

Figure 20 shows $\mathrm{d}\bar{\tau}/\mathrm{d}\ln M_{\rm L}$ for this given minimum delay. Just as in the case of a point mass, the redshift distribution that follows SFH, thereby characterising FRBs at higher redshifts, results in a higher $\mathrm{d}\bar{\tau}/\mathrm{d}\ln M_{\rm L}$.

Part of the optical depth in Figure 20 comes from halo masses that are below the different free streaming masses. The optical depth is dominated by the effects of higher mass halos where there is no significant difference between CDM and WDM.

3.4.1 WDM Particle Mass

By integrating $\mathrm{d}\bar{\tau}/\mathrm{d}\ln M_{\rm L}$ over halo mass $M_{\rm L}$, we can see how the integrated optical depth $\bar{\tau}$ changes with WDM particle mass. This is done with $\Delta t_{\rm min}$ = 1 ms. Since the time delay must be smaller than 24 hours to be able to distinguish a lensed FRB from a repeater, we integrate up until the characteristic mass scale $M_{\rm L}(24\ \mathrm{hours}) \sim 10^{11}$ M$_\odot$.

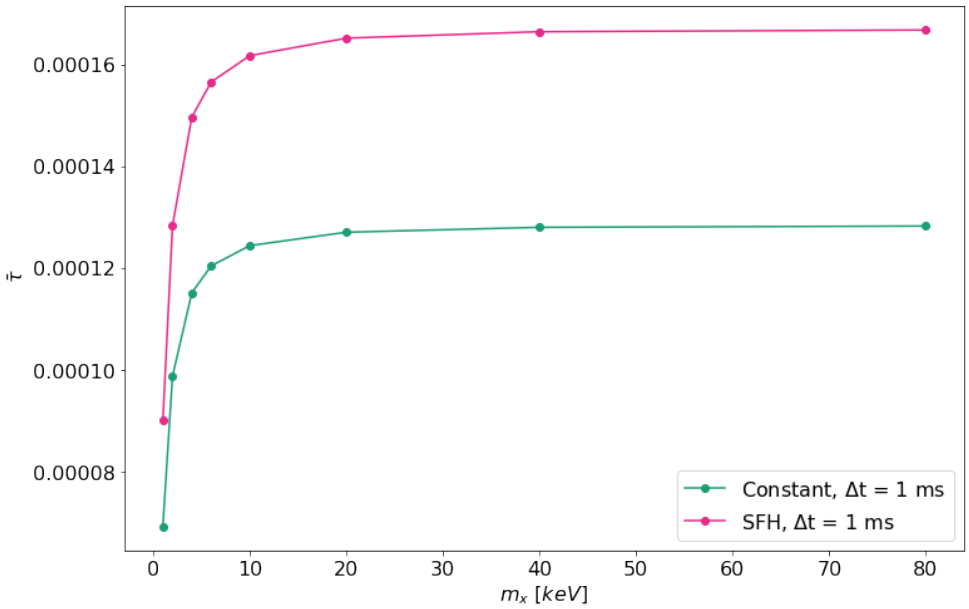

Figure 21: Integrated optical depth $\bar{\tau}$ for a population of FRBs with a constant comoving density and a population that follows SFH.

Figure 21 show $\mathrm{d}\bar{\tau}$ for different WDM particle masses $m_{\rm X}$ integrated up to the characteristic mass scale $M_{\rm L}(24\ \mathrm{hours})$. In the case of dark matter halos, the integrated optical depth is 10^{-4}. This is $\sim 10^2$ times smaller than in the case of PBHs. This results in weaker constraints for halos than for PBHs. The difference in optical for the different types of WDM is on 10^{-5} scale, and

for a realistic FRB detection rate of 10^4 FRBs per year, it will be difficult to separate the CDM and WDM.

3.4.2 Time Delay on the Scale of 10 μs

Since ASKAP is now able to distinguish FRB temporal features on a 10 μs scale, it is interesting to consider how a minimum gravitational time delay of 10 μs will affect the integrated optical depth $\mathrm{d}\bar{\tau}/\mathrm{d}\ln M_{\mathrm{L}}$. From Figure 22, we see that this corresponds to a minimum lensing mass of $\sim 10^3$ $\mathrm{M}_\odot$. Since the difference in HMF for different particle masses of WDM is most significant for smaller masses (cf. Figure 6), this could potentially make the optical depths for each type of WDM more distinct.

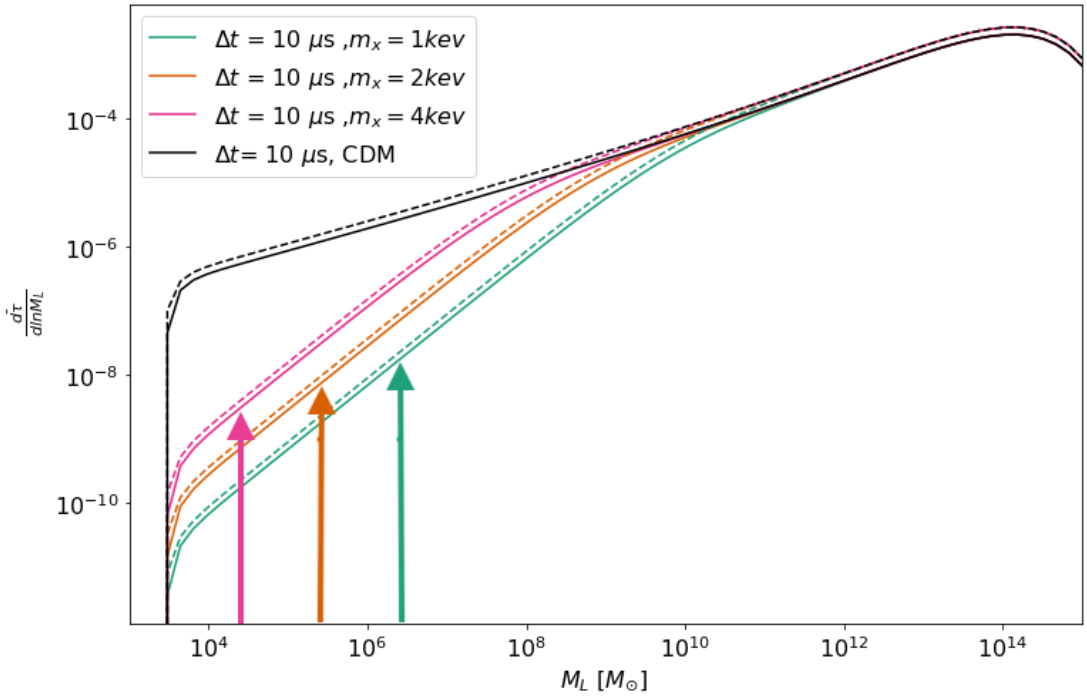

Figure 22: $\mathrm{d}\bar{\tau}/\mathrm{d}\ln M_{\mathrm{L}}$ for a population of FRBs with a constant comoving density (solid) and a population that follows SFH (dashed). Computed for a minimum time delay of $\Delta t = 10$ μs. The arrows indicate the free streaming mass of the different WDM particles. Below these masses the optical depth is zero.

Similar to the results for a minimum time delay of $\Delta t = 1$ ms, a large part of the optical depth in Figure 22 comes from halo masses that are below the different free streaming masses. The optical depth is still mostly dominated by the effects of higher mass halos and it is difficult to distinguish between CDM and WDM.

3.5 CHIME Twin Peaks

In the data released by CHIME/FRB in June 2021, there are four categories of FRB morphology, with one comprising complex multi-peak FRBs where the peaks can have different amplitudes (Pleunis et al., 2021). Some of these multi-peak FRBs can potentially be interpreted as candidates for lensed FRBs.

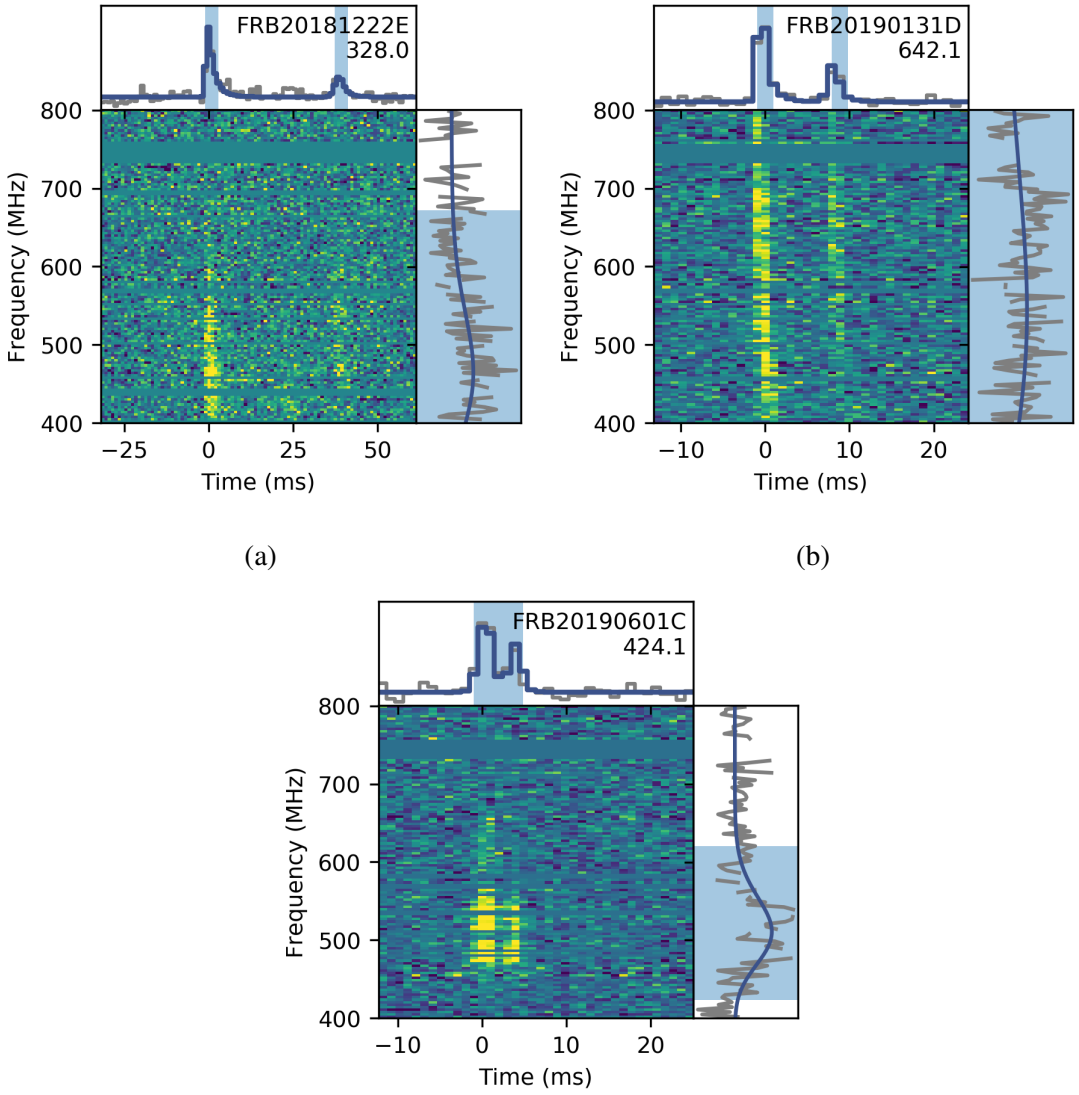

(a) (b)

(c)

Figure 23: Figures adapted from CHIME/FRB Collaboration et al. (2021).

We consider FRB20181222E, FRB20190131D and FRB20190601C, displayed in Figure 23, as three possible lensed FRB candidates as the twin peaks have a similar shape and a similar frequency pattern.

3.5.1 Primordial Black Hole

We can determine the mass of the point lens from the observed parameters R, Δt, and $z_{\rm L}$ in the following way (Chen et al., 2021):

$$M_{\rm L}(1+z_{\rm L}) = \frac{c^3 \Delta t}{2G} \frac{\sqrt{R}}{R-1+\sqrt{R}\ln R}. \tag{66}$$

The flux ratio R and time delay Δt can be estimated from the figures for a rough order of magnitude estimate. We do not have an estimate of $z_{\rm L}$, but we can find the maximum lens mass given that the lens is within the Milky Way at $z = 0$. The minimum lens mass will be right by the FRB source at $z_{\rm S}$ that can be estimated from the dispersion measure, as shown in the previous sections.

Name	Δt [ms]	$R_{\rm f}$	$DM_{\rm excess}$ [pc cm^{-3}]	z	$M(1+z_{\rm L})$ [M$_\odot$]
FRB20181222E	39	2.96	268.1	0.335	1779.5681
FRB20190131D	8	1.95	574.6	0.718	602.312
FRB20190601C	4	1.34	237.7	0.297	692.37802

Table 1: Estimates of $M_{\rm L}$ for the lensed FRB candidates if the lens is a point mass.

These correspond to black hole masses if we assume a lensing interpretation of the twin peak signal.

3.5.2 Dark Matter Halo

The velocity dispersion can be calculated from the time delay Δt, the estimated redshift z, and flux ratio $R_{\rm f}$:

$$v^4(1+z_{\rm L}) = \frac{c^5 \Delta t}{16\pi^2} \frac{D_{\rm S}}{D_{\rm L} D_{\rm LS}} \frac{R-1}{R-1+\sqrt{9R^2-10R+1}}. \tag{67}$$

The corresponding virial mass can be calculated from the velocity dispersion:

$$v = \left(\frac{100}{3} G^3 M^2 \pi \rho_{\rm c}\right)^{\frac{1}{6}}, \tag{68}$$

with

$$\rho_{\rm c} = \frac{3H^2(z)}{8\pi G}. \tag{69}$$

The mass will depend on the redshift of the lens $z_{\rm L}$, as this enters the expression for the angular diameter distances (cf. Equation (26)). For a similar estimate, we calculate $M_{\rm L}$ for $z_{\rm L} = z_{\rm S}/2$.

Name	Δt [ms]	$R_{\rm f}$	$DM_{\rm excess}$ [pc cm^{-3}]	z	$M(z_{\rm S}/2)$ [M$_\odot$]
FRB20181222E	39	2.96	268.1	0.335	1.4×10^7
FRB20190131D	8	1.95	574.6	0.718	2×10^6
FRB20190601C	4	1.34	237.7	0.297	4×10^6

Table 2: Estimates of $M_{\rm L}$ for the lensed FRB candidates for an SIS lens.

If we examine the possible lens masses $M_{\rm L}$ in Table 1, the smallest $M_{\rm L}$ at $z_{\rm L}$ is above 100 M$_\odot$. As previously stated, dark matter in the form of PBHs is ruled out at above 100 M$_\odot$ such as these. If the lens is described by an SIS model, we find $M_{\rm L}$ in Table 2 on the scale of 10^6 to 10^7 M$_\odot$.

4 Discussion

We proposed two different lens models that will result in time delays with a minimum delay of 1 ms and 10 μs, and a maximum delay of $\sim$ 24 hours. These time delays will be detectable for FRB observations. Both MACHOs with mass of 20-100 $M_\odot$, as well as dark matter halos on a mass of 10^6 $M_\odot$, will result in a time delay on ms scale. Gravitational lensing by both a point source lens and a singular isothermal sphere will result in two lensed images. So how can we distinguish between a black hole at 20 $M_\odot$ and a CDM halo of 10^6 $M_\odot$? If both lens models result in two images with a similar temporal separation, how do we tell them apart? An SIS is a highly idealised model for a halo. In reality, halos will not be perfectly spherical. In the case of a more elliptical halo, more than two images will be produced from the lensed event. If we observe a lensed FRB with only two images, it might be more likely that the lens is a point mass. However, in the case of four images from elliptical halos, some of the images might be too faint for detection and we can only observe the two brightest images. As a consequence, we might not know if we have two or more images. This makes it really difficult to distinguish between point mass lenses of smaller masses and SIS lenses of larger masses. On another note, we find the optical depth to be lower for dark matter halos compared to dark matter in the form of PBHs. In the case where all dark matter ($f_{\rm DM}$=1) is in the form of PBHs we expect that $\sim$130 out of 10^4 FRBs will be lensed compared to $\sim$1 if all dark matter is in halos. The constraints are comparable if we consider that the fraction of dark matter in the form of PBHs is $f_{\rm DM} = 10^{-2}$.

4.1 Redshift Distribution and Dispersion Measure

The redshift distribution $N(z)$ of FRBs has a significant impact on the integrated optical depth $\bar{\tau}$ (cf. Equation (50)). This effect is clearly evident in Figure 18. The value of $z_{\rm cut}$ has a substantial effect on $\bar{\tau}$. The further out an FRB is emitted, the more probable is the possibility of a lens object intervening on its way to the observer on Earth. Let us recall that for the FRBs in the FRB catalogue by Petroff et al. (2016), the estimated $DM_{\rm IGM}$ and the associated redshifts z are listed without any estimation of $DM_{\rm host}$. The redshifts must be thought of as maximum redshifts.

However, for the CHIME/FRB catalogue data, $DM_{\rm host}$ = 100 pc cm^{-3} is subtracted from the $DM_{\rm excess}$. It is still worth noting that this is a higher estimate of z.

Since it is cumbersome to estimate redshifts from the dispersion measure, an accurate red-

shift distribution requires the localisation of the host galaxy. There are currently 19 FRBs with an identified host (Heintz et al., 2020). Most of these FRBs have been detected with ASKAP and, therefore, have lower redshifts. Only by employing a distribution of FRBs with known hosts might give a more certain distribution, but it will be limited by a lower $z_{\rm cut}$.

4.2 Repeaters and Detections

From the current data, a small fraction of the FRB detections comprises repeating FRBs. Most of them repeat more than just once. The time between the repeating bursts can vary from a day to more than a year in between. Very few repeaters recur within 24 hours, and even fewer repeat only once. However, some of them repeat on shorter scales of hours, minutes or even milliseconds. This might make it difficult to produce a clear cut-off between lensed FRBs and repeating FRBs.

Interestingly enough, in the recent publications by the CHIME collaboration (Pleunis et al., 2021), it seems that the morphology is quite different when we compare single bursts to repeaters. When we study larger data samples, single bursts and repeaters tend to differ on average when we compare their time duration and bandwidth. More information on this, in particular, more statistics, could classify a "not yet repeating" burst in the future as a single or repeating burst by comparing it to the known morphologies.

4.3 Experiments

The different experiments CHIME, Parkes and ASKAP all possess different advantages when it comes to observations of lensed FRBs.

Throughout the year of 2018 to 2019, CHIME has detected more than 500 FRBs and more than 20 repeaters. As of now, it seems probable that CHIME will dominate FRB detections in the near future. Before the publication of the CHIME-FRB catalogue in June 2021, there were around 140 FRB detections since the Lorimer burst in 2007 (Petroff et al., 2016). The CHIME experiment has a higher cut-off redshift of $z_{\rm cut} \approx 0.5$ compared to $z_{\rm cut} = 0.25$ from pre-2021 data. Parkes has the advantage of a higher cut-off redshift at $z_{\rm cut} = 0.8$ that results in a higher optical depth. This allowed Parkes to dominate the early FRB data collections, but is for now not comparable in number to CHIME.

ASKAP has the ability to resolve temporal features on the scale of 10 μs. This is particularly interesting in the case of WDM, as this corresponds to a smaller mass of around 10^4 $M_\odot$, and here, we expect to see a larger difference in optical depth when we compare various particle masses. The improved temporal resolution of ASKAP is not as useful in the case of dark matter as PBHs as the time delay would correspond to a smaller mass than the allowed range of 20-100 $M_\odot$. One remarkable strength of ASKAP is that its precision is sufficient enough to locate the FRB host galaxies. This means that we can know the redshift of the source instead of inferring it from the dispersion measure. From the host galaxy redshift, we can determine the IGM dispersion measure and calculate the host galaxy dispersion measure. When the data sample from ASKAP is sufficient for statistical analysis, we can use this for a better estimation of $DM_{\rm host}$ for the other experiments.

4.4 Sub-halos

In the calculations of the lensing probability, we have not taken the effects of sub-halos into account:

$$\frac{{\rm d}n_{\rm total}}{{\rm d}\ln M_{\rm host}} = \frac{{\rm d}n_{\rm host}}{{\rm d}\ln M_{\rm host}} + \frac{{\rm d}n_{\rm sub}}{{\rm d}\ln M_{\rm host}}. \tag{70}$$

We know the USMF:

$$F\left(\frac{M_{\rm sub}}{M_{\rm host}}\right) = \frac{{\rm d}n_{\rm sub}}{{\rm d}\ln(M_{\rm sub}/M_{\rm host})} = a\left(\frac{M_{\rm sub}}{M_{\rm host}}\right)^b \exp\left[-c\left(\frac{M_{\rm sub}}{M_{\rm host}}\right)^d\right]. \tag{17}$$

We can then find the sub-halo mass function by integrating the USMF multiplied with the HMF:

$$\frac{{\rm d}n_{\rm sub}}{{\rm d}\ln M_{\rm host}} = \int_{\ln M_{\rm sub,min}}^{\ln M_{\rm host,max}} \frac{{\rm d}n_{\rm host}}{{\rm d}\ln M_{\rm sub}/M_{\rm host}} \cdot \frac{{\rm d}n_{\rm host}}{{\rm d}\ln M_{\rm host}} {\rm d}\ln M_{\rm host}. \tag{71}$$

For comparison, we plot the sub-HMF, the HMF and the total HMF in Figure 24. Figure 25 is zoomed in on the lower mass scale of what we consider in our results. If we compare the HMF of host halos alone to that with added sub-halos, it appears that there is less than a factor of 2 difference between the HMFs.

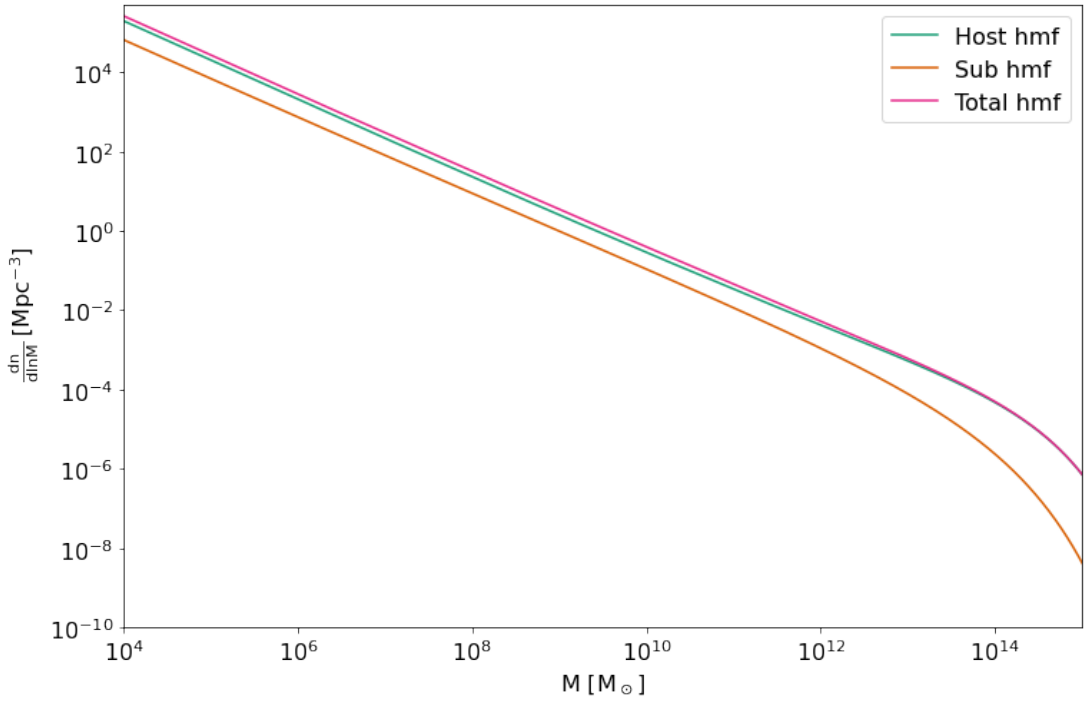

Figure 24: Comparison of the host halo HMF for CDM, sub-halo HMF, and the total HMF for CDM.

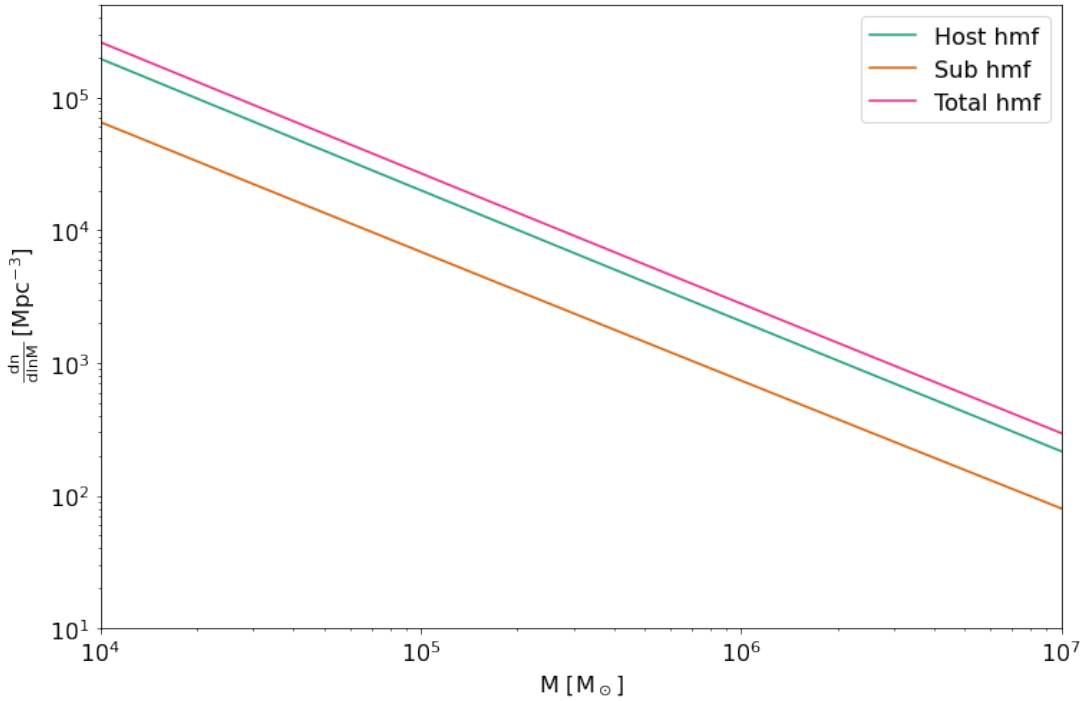

Figure 25: Comparison of the host halo HMF for CDM, sub-halo HMF, and the total HMF for CDM for $M_{\rm halo} = 10^4 - 10^7$ M$_\odot$.

For a more intuitive comparison, we plot the difference in HMF and and the total HMF including sub-halos in Figure 26.

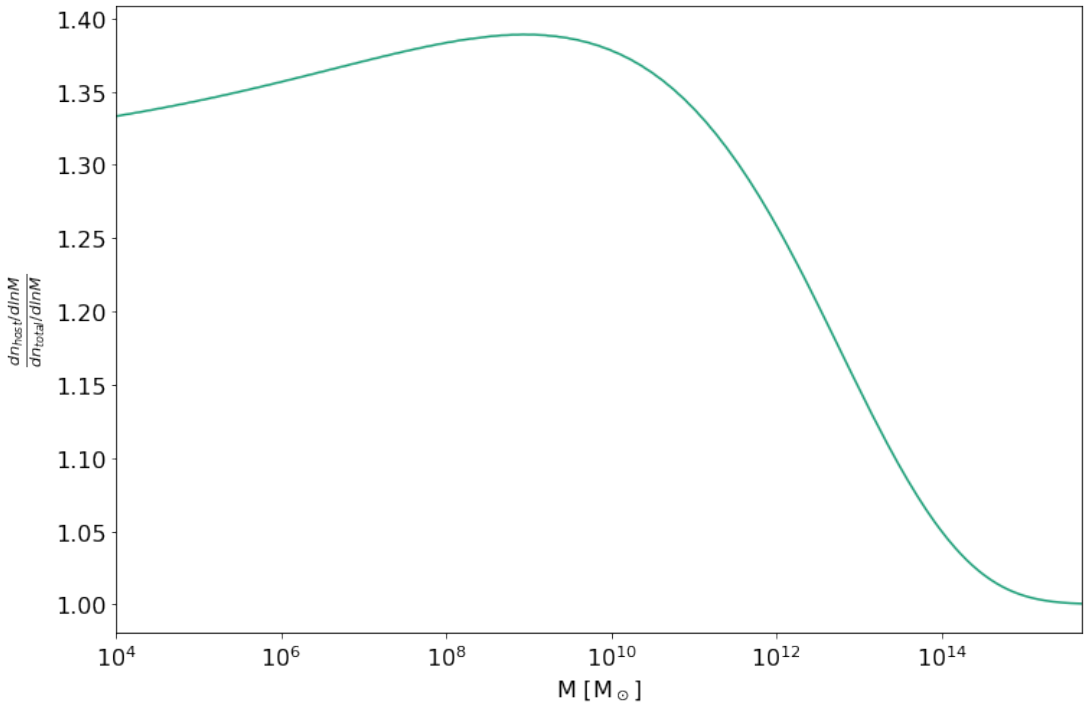

Figure 26: Difference in HMF for CDM excluding sub-halos and HMF including HMF for CDM.

From Figure 26, it is evident that the effects of sub-halos result in an increase by $\sim$ 30 per cent. It is worth emphasising that this is the absolute maximum number of sub-halos as the USMF assumes that all accreted mass is conserved in sub-halos. The effects are most prevalent for halos between 10^5–10^{12} $M_\odot$, which exactly corresponds to the mass window considered in this work. However, this boost yields a maximum of $\sim$ 30 per cent more halos, with the actual increase likely to be even less.

4.5 Plasma Lensing

As mentioned in Chapter 2, concentrations of electrons in cold plasma can behave similarly to a lens and cause a chromatic time delay in radio signals such as FRBs. The large dispersion measures of FRBs means that they do propagate through a cold plasma, but the latter is generally assumed to be a smooth distribution in the IGM. Moreover, within a dark matter halo, we might also encounter some plasma that could result in another lensing effect as an FRB passes by.

If we compare the plasma potential in Equation (61) with the gravitational lensing potential, we can estimate if plasma lensing will have a noticeable effect on a gravitationally lensed FRB:

$$\psi_{\text{plasma}}(x) = -\frac{D_{\text{LS}}}{D_{\text{L}} D_{\text{S}}} \frac{r_e \lambda^2}{2\pi} N_e(x) \tag{72}$$

$$\psi_{\text{gravitational}}(x) = \frac{D_{\text{LS}}}{D_{\text{L}} D_{\text{S}}} \frac{4GM}{c^2} \ln |x| \tag{73}$$

We consider a typical halo with a mass of 10^6 $M_\odot$, a typical wavelength for an FRB as 1 m, and a position $x = 1.5$. For the dispersion measure $N_e(x)$, we assume a similar electron distribution for the Milky way (100 pc cm^{-3}) and scale as if the density in the halo is the same as from a halo in Milky Way of 10^{11} $M_\odot$ to a halo at 10^6 $M_\odot$.

$$\frac{\frac{r_e \lambda^2}{2\pi} N_e(x)}{\frac{4GM}{c^2} \ln |x|} \sim 10^{-6}. \tag{74}$$

The effects of plasma lensing would in this case be negligible.

4.6 Which kind of black hole?

If a lensed FRB is successfully identified as being lensed by a point mass, i.e. a black hole, it is still not obvious whether it is a primordial black hole or a stellar black hole. Since the first LIGO detection, the origin of the detected binary black holes (BBHs) has been up for debate.

A counter argument to Bird et al. (2016), who claimed that LIGO detected dark matter in the form of PBHs, is that the $\sim$ 30 $M_\odot$ black holes have formed through previous mergers of stellar black holes (Zevin et al., 2021). Supporters of the PBH hypothesis point out how the misalignment of the spin orientation for BBH suggests that the black holes are unlikely to be exclusive products of previous black hole gravitational capture. However, if BBHs are formed by such capture events, this likely takes place in very dense stellar environments, such as globular clusters, and such environments could result in random spin orientations. However, it is questionable if all BBHs are likely to have a misaligned spin orientation.

There is no trivial way to distinguish between stellar and primordial black holes. If we detect a single black hole, it is impossible to know the origin. Nevertheless, if we observe a statistically significant number of BBHs with M $>$ 20 $M_\odot$ and with a misaligned spin orientation, they would represent a plausible candidate of dark matter in the form of PBHs.

5 Conclusion

FRBs currently exhibit a temporal resolution on ms - and in some case 10 μs scales. This quality means that lensed FRBs can be detected for minimum time delays on similar scales. This is particularly interesting when you consider dark matter in the form of PBHs, as these are possible in a mass range from 20 to 100 $M_\odot$. PBHs will act as a point mass lens and the time delay that corresponds to a lens mass in this range is exactly around 1 ms. For dark matter in halos, the corresponding mass scale is around 10^6 $M_\odot$. At this mass, the HMF predicts a difference in the number of halo for CDM and different particle masses of WDM. This difference will result in different optical depths for different types of dark matter.

For dark matter in the form of PBHs, we find that for a redshift distribution of FRBs that are similar to the recently published CHIME/FRB catalogue, if less than 1 out of 1 out 10^4 FRBs are lensed, we can constrain the dark matter in the form of PBHs with $M_{\rm L} > 10$ $M_\odot$ to less than 0.8 percent.

For dark matter halos, we find the optical depth to be about a 100 times smaller than for PBHs with $f_{\rm DM} = 1$. The higher mass halos dominate the optical depth and the difference in CDM and WDM is essentially undetectable. In a sample of 10^4 FRBs about 1 FRB is likely to be lensed by a dark matter halo.

The optical depth depends on the redshift distribution, where a larger $z_{\rm cut}$ result in a greater probability of lensed FRBs. $z_{\rm cut}$ is characteristic for each telescope's sensitivity. As of now, data in the CHIME/FRB catalogue dominates FRB detection and suggests $z_{\rm cut} = 0.5$, however it is plausible that future FRB experiments can go deeper into the Universe and observe FRBs at redshift of a similar sensitivity as Parkes with $z_{\rm cut} = 0.8$, but with a higher detection rate similar to CHIME. Sub-halos within dark matter halos might also boost the optical depth and result in stricter constraints on dark matter in the form of halos. If the temporal resolution continue to be improved, this might also boost the expected number of lensed FRBs. As we are just scratching the surface, future FRB experiments will potentially result in a higher optical depth that will make it possible to characterise the nature of dark matter.

References

Abbott B. P., et al., 2016, Physical Review X, 6, 041015

Bannister K. W., et al., 2017, ApJ, 841, L12

Bird S., Cholis I., Muñoz J. B., Ali-Haïmoud Y., Kamionkowski M., Kovetz E. D., Raccanelli A., Riess A. G., 2016, Phys. Rev. Lett., 116, 201301

Bond J. R., Kofman L., Pogosyan D., 1996, Nature, 380, 603

CHIME/FRB Collaboration et al., 2018, ApJ, 863, 48

CHIME/FRB Collaboration et al., 2021, arXiv e-prints, p. arXiv:2106.04352

Caleb M., Flynn C., Bailes M., Barr E. D., Hunstead R. W., Keane E. F., Ravi V., van Straten W., 2016, MNRAS, 458, 708

Carr B. J., Hawking S. W., 1974, MNRAS, 168, 399

Carr B., Kühnel F., 2020, Annual Review of Nuclear and Particle Science, 70, 355

Carr B., Kohri K., Sendouda Y., Yokoyama J., 2020, arXiv e-prints, p. arXiv:2002.12778

Chen X., Shu Y., Zheng W., Li G., 2021, ApJ, 912, 134

Congdon A. B., Keeton C., 2018, Principles of Gravitational Lensing: Light Deflection as a Probe of Astrophysics and Cosmology

Connor L., Lin H.-H., Masui K., Oppermann N., Pen U.-L., Peterson J. B., Roman A., Sievers J., 2016, MNRAS, 460, 1054

Cordes J. M., 2004, in Clemens D., Shah R., Brainerd T., eds, Astronomical Society of the Pacific Conference Series Vol. 317, Milky Way Surveys: The Structure and Evolution of our Galaxy. p. 211

Deng W., Zhang B., 2014, ApJ, 783, L35

Heintz K. E., et al., 2020, ApJ, 903, 152

Hinshaw G., et al., 2013, ApJS, 208, 19

Hogg D. W., 1999, arXiv e-prints, pp astro–ph/9905116

James C. W., et al., 2019, PASA, 36, e009

Li Y., Mo H., 2009, arXiv e-prints, p. arXiv:0908.0301

Longair M. S., 2007, Galaxy formation. Springer Science & Business Media

Lorimer D. R., Kramer M., 2012, Handbook of Pulsar Astronomy

Lorimer D. R., Bailes M., McLaughlin M. A., Narkevic D. J., Crawford F., 2007, Science, 318, 777

Macquart J.-P., et al., 2010, PASA, 27, 272

Madau P., Diemand J., Kuhlen M., 2008, ApJ, 679, 1260

Muñoz J. B., Kovetz E. D., Dai L., Kamionkowski M., 2016, Phys. Rev. Lett., 117, 091301

Murray S. G., Power C., Robotham A. S. G., 2013a, Astronomy and Computing, 3, 23

Murray S. G., Power C., Robotham A. S. G., 2013b, Astronomy and Computing, 3, 23

Pace F., Waizmann J. C., Bartelmann M., 2010, MNRAS, 406, 1865

Petroff E., et al., 2015, MNRAS, 447, 246

Petroff E., et al., 2016, PASA, 33, e045

Petroff E., Hessels J. W. T., Lorimer D. R., 2019, A&A Rev., 27, 4

Petroff E., Hessels J. W. T., Lorimer D. R., 2021, arXiv e-prints, p. arXiv:2107.10113

Pleunis Z., et al., 2021, arXiv e-prints, p. arXiv:2106.04356

Press W. H., Schechter P., 1974, ApJ, 187, 425

Rubin V. C., Ford W. Kent J., 1970, ApJ, 159, 379

Ryden B., 2003, Introduction to cosmology

Sammons M. W., Macquart J.-P., Ekers R. D., Shannon R. M., Cho H., Prochaska J. X., Deller A. T., Day C. K., 2020, ApJ, 900, 122

Schneider A., Smith R. E., Macciò A. V., Moore B., 2012, MNRAS, 424, 684

Shapiro I. I., 1964, Phys. Rev. Lett., 13, 789

Tendulkar S. P., et al., 2017, ApJ, 834, L7

Thornton D., et al., 2013, Science, 341, 53

Tinker J., Kravtsov A. V., Klypin A., Abazajian K., Warren M., Yepes G., Gottlöber S., Holz D. E., 2008, ApJ, 688, 709

Viel M., Lesgourgues J., Haehnelt M. G., Matarrese S., Riotto A., 2005, Phys. Rev. D, 71, 063534

Wagner J., Er X., 2020, arXiv e-prints, p. arXiv:2006.16263

White M., 2001, A&A, 367, 27

Zasov A. V., Saburova A. S., Khoperskov A. V., Khoperskov S. A., 2017, Physics Uspekhi, 60, 3

Zevin M., et al., 2021, ApJ, 910, 152

Zwicky F., 1933, Helvetica Physica Acta, 6, 110